

SPDIM: SOURCE-FREE UNSUPERVISED CONDITIONAL AND LABEL SHIFT ADAPTATION IN EEG

Shanglin Li^{1,2,†}, Motoaki Kawanabe^{2,3} & Reinmar J. Kobler^{2,3,†}

¹ Nara Institute of Science and Technology (NAIST), Nara, Japan

² Department of Dynamic Brain Imaging, ATR, Kyoto, Japan

³ Center for Advanced Intelligence Project, RIKEN, Tokyo, Japan

† Equal contribution

{shanglin,kawanabe,reinmar.kobler}@atr.jp

ABSTRACT

The non-stationary nature of electroencephalography (EEG) introduces distribution shifts across domains (e.g., days and subjects), posing a significant challenge to EEG-based neurotechnology generalization. Without labeled calibration data for target domains, the problem is a source-free unsupervised domain adaptation (SFUDA) problem. For scenarios with constant label distribution, Riemannian geometry-aware statistical alignment frameworks on the symmetric positive definite (SPD) manifold are considered state-of-the-art. However, many practical scenarios, including EEG-based sleep staging, exhibit label shifts. Here, we propose a geometric deep learning framework for SFUDA problems under specific distribution shifts, including label shifts. We introduce a novel, realistic generative model and show that prior Riemannian statistical alignment methods on the SPD manifold can compensate for specific marginal and conditional distribution shifts but hurt generalization under label shifts. As a remedy, we propose a parameter-efficient manifold optimization strategy termed SPDIM. SPDIM uses the information maximization principle to learn a single SPD-manifold-constrained parameter per target domain. In simulations, we demonstrate that SPDIM can compensate for the shifts under our generative model. Moreover, using public EEG-based brain-computer interface and sleep staging datasets, we show that SPDIM outperforms prior approaches.

1 INTRODUCTION

Electroencephalography (EEG) measures multi-channel electric brain activity from the human scalp (Niedermeyer & da Silva, 2005) and can reveal cognitive processes (Pfurtscheller & Da Silva, 1999), emotion states (Suhaimi et al., 2020), and health status (Alotaiby et al., 2014). Neurotechnology and brain-computer interfaces (BCI) aim to extract patterns from the EEG activity that can be utilized for various applications, including rehabilitation and communication (Wolpaw et al., 2002). Despite their capabilities, they currently suffer from a low signal-to-noise ratio (SNR), low specificity, and non-stationarities manifesting as distribution shifts across days and subjects (Fairclough & Lotte, 2020).

For EEG-based neurotechnology, distribution shifts have been traditionally mitigated by collecting labeled calibration data and training domain-specific models (Lotte et al., 2018), limiting neurotechnology utility and scalability (Wei et al., 2022). As an alternative, domain adaptation (DA) learns a model from one or multiple source domains that performs well on different (but related) target domain(s), offering principled statistical learning approaches with theoretical guarantees (Ben-David et al., 2010; Hoffman et al., 2018). Within the BCI field, DA primarily addresses cross-session and cross-subject transfer learning (TL) problems (Wu et al., 2020), aiming to achieve robust generalization across domains (e.g., sessions and subjects) without supervised calibration data.

BCIs that generalize across domains without requiring labeled calibration data are one of the grand challenges in EEG-based BCI research (Fairclough & Lotte, 2020; Wolpaw et al., 2002). Since target domain data is typically unavailable during training, the problem corresponds to a source-free unsu-

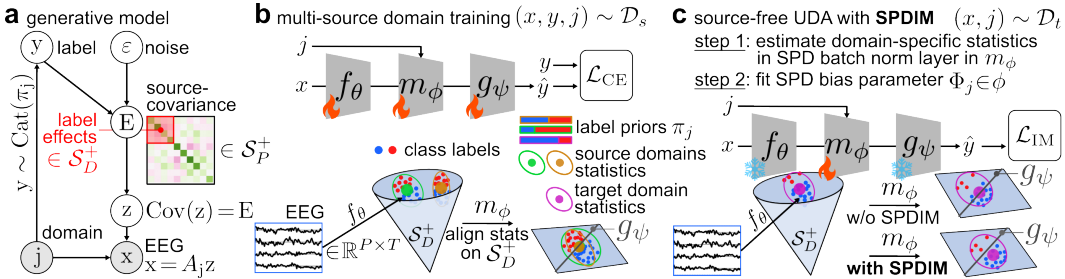


Figure 1: **Framework Overview.** **a**, EEG data x is generated by mixing source signals z with unknown, linear forward models A_j . A submanifold S_D^+ of the sources’ covariance matrices $E \in S_P^+$ encodes information about the label y . Domain-specific label priors π_j and forward models A_j introduce label and conditional distribution shifts, respectively. **b**, Multi-source domain training, utilizes balanced batch sampling and the end-to-end latent alignment framework proposed in (Kobler et al., 2022a). **c**, Proposed SPDIM framework. After latent alignment of marginal distributions (step 1), SPDIM uses the information maximization (IM) loss to fit a bias parameter $\Phi_j \in S_D^+$ (step 2), and thereby counteract over-corrections in step 1 that are driven by label shifts.

pervised domain adaptation (SFUDA) problem (Liu et al., 2021; Yang et al., 2021). For this problem class, Riemannian geometry-aware statistical alignment frameworks (Barachant et al., 2011) operating with symmetric, positive definite (SPD) matrix-valued features are considered state-of-the-art (SoA) in cross-domain (Roy et al., 2022; Mellot et al., 2023) generalization. They offer several advantageous properties, such as invariance to linear mixing, that are suitable for EEG data (Congedo et al., 2017), as well as consistent (Sabbagh et al., 2020) and inherently interpretable (Kobler et al., 2021) estimators for generative models with a log-linear relationship between the power of latent sources and the labels. Additionally, Collas et al. (2024) suggests that a linear mapping exists between the source and target domains in Riemannian geometry framework. To facilitate generalization across domains, statistical alignment frameworks aim to align first (Zanini et al., 2017; Yair et al., 2019) and second (Rodrigues et al., 2019; Kobler et al., 2022a) order moments, denoted Fréchet mean and variance on Riemannian manifolds. Once the moments are aligned, a model trained on source domains typically generalizes to related target domains (Zanini et al., 2017; Wei et al., 2022; Kobler et al., 2022a; Ju & Guan, 2022; Mellot et al., 2024).

Although infrequently studied, many applications, including EEG-based sleep staging, exhibit label shift (Thölke et al., 2023). Under label shift, aligning the moments of the marginal feature distributions can increase the generalization error (Bakas et al., 2023). To address various sources of distribution shifts in EEG, an SFUDA approach that can deal with additional label shifts is required. Machine learning literature offers several frameworks for SFUDA problems with label shift (Li et al., 2021; Liang et al., 2024), but few have been applied to EEG data. For example, Li et al. (2023) employed the information maximization (Shi & Sha, 2012) objective for cross-domain generalization. Within Riemannian geometry methods, Mellot et al. (2024) studied an EEG-based age regression problem and proposed a framework to facilitate generalization across populations with different prior distributions.

Here, we propose a geometric deep learning framework to tackle SFUDA classification problems under distribution shifts, including label shift. We introduce a realistic generative model with a log-linear relationship between the covariance of latent sources and the labels (Figure 1a). We provide theoretical analyses showing that prior Riemannian statistical alignment methods (Figure 1b) on the SPD manifold can compensate for the conditional distribution shifts introduced in our model but hurt generalization under additional label shifts. As a remedy, we propose a parameter-efficient manifold optimization strategy termed SPDIM. SPDIM employs the information maximization principle to learn a domain-specific SPD-manifold-constrained bias parameter to compensate over-corrections introduced via aligning the Fréchet mean (Figure 1c).

2 PRELIMINARIES

2.1 SFUDA SCENARIO

Let y and x denote random variables representing the true labels and associated features, and let $p_j(y)$ and $p_j(x|y)$ be the prior and conditional probability distributions for domain j . In the transfer learning scenario considered here, we assume that the class priors $\pi_j := p_j(y)$ can be different from each other, as well as specific shifts in the conditional distributions $p_j(x|y)$. We consider a labeled source dataset $\mathcal{D}_s = \{(x_i, y_i, j_i) | x_i \in \mathcal{X}_s, y_i \in \mathcal{Y}_s, j_i \in \mathcal{J}_s\}_{i=1}^{L_s}$ and an unlabeled target dataset $\mathcal{D}_t = \{(x_i, j_i) | x_i \in \mathcal{X}_t, y_i \in \mathcal{Y}_t, j_i \in \mathcal{J}_t\}_{i=1}^{L_t}$, where y_i and j_i (or $j(i)$ if used as suffix) indicate the associated label and domain for each example i . We additionally assume that both datasets share the feature space (i.e., $\mathcal{X}_s = \mathcal{X}_t = \mathcal{X}$), contain the same classes (i.e., $\mathcal{Y}_s = \mathcal{Y}_t = \mathcal{Y}$), and comprise examples from different domains (i.e., $\mathcal{J}_s \cap \mathcal{J}_t = \emptyset$). The goal is to transfer the knowledge learned from \mathcal{D}_s to \mathcal{D}_t via first learning a source decoder h_s within hypothesis class \mathcal{H} and then use h_s and the unlabeled target dataset \mathcal{D}_t to learn $h_t \in \mathcal{H}$.

2.2 RIEMANNIAN GEOMETRY ON \mathcal{S}_D^+

The SPD manifold $\mathcal{S}_D^+ = \{C \in \mathbb{R}^{D \times D} : C^T = C, C \succ 0\}$ together with an inner product on its tangent space $\mathcal{T}_C \mathcal{S}_D^+$ at each point $C \in \mathcal{S}_D^+$ forms a Riemannian manifold. Tangent spaces have Euclidean structure with easy-to-compute distances, which locally approximate Riemannian distances on \mathcal{S}_D^+ (Absil et al., 2008). In this work, we consider the affine invariant Riemannian metric (AIRM) $g_C^{\text{AIRM}}(S_1, S_2) = \text{Tr}(C^{-1} S_1 C^{-1} S_2)$ as the inner product, which gives rise to the following distance (Bhatia, 2009):

$$\delta(C_1, C_2) = \|\log(C_1^{-\frac{1}{2}} C_2 C_1^{-\frac{1}{2}})\|_F \quad (1)$$

where C_1 and C_2 are two SPD matrices, $\text{Tr}(\cdot)$ denotes the trace, $\log(\cdot)$ the matrix logarithm, and $\|\cdot\|_F$ the Frobenius norm. For a set of points $\mathcal{C} = \{C_i \in \mathcal{S}_D^+\}_{i \leq M}$, the Fréchet mean is defined as the minimizer of the average squared distances:

$$\bar{C} = \arg \min_{G \in \mathcal{S}_D^+} \nu_G(\mathcal{C}) = \arg \min_{G \in \mathcal{S}_D^+} \frac{1}{M} \sum_{i=1}^M \delta^2(G, C_i) \quad (2)$$

For $M = 2$, there exists a closed form solution:

$$\bar{C} = \arg \min_{G \in \mathcal{S}_D^+} \nu_G(\{C_1, C_2\}) = C_1 \#_t C_2 |_{t=\frac{1}{2}} = C_1^{\frac{1}{2}} \left(C_1^{-\frac{1}{2}} C_2 C_1^{-\frac{1}{2}} \right)^t C_1^{\frac{1}{2}} \Big|_{t=\frac{1}{2}} \quad (3)$$

where parameter $t \in [0, 1]$ smoothly interpolates along the geodesic $C_1 \#_t C_2$ (i.e., the shortest path) connecting both points.

The logarithmic map $\text{Log}_{\bar{C}} : \mathcal{S}_D^+ \rightarrow \mathcal{T}_{\bar{C}} \mathcal{S}_D^+$ and exponential map $\text{Exp}_{\bar{C}} : \mathcal{T}_{\bar{C}} \mathcal{S}_D^+ \rightarrow \mathcal{S}_D^+$ project points between the manifold and the tangent space at point \bar{C} :

$$\text{Log}_{\bar{C}}(C_i) = \bar{C}^{-\frac{1}{2}} \log(\bar{C}^{-\frac{1}{2}} C_i \bar{C}^{-\frac{1}{2}}) \bar{C}^{\frac{1}{2}} \quad (4)$$

$$\text{Exp}_{\bar{C}}(S_i) = \bar{C}^{\frac{1}{2}} \exp(\bar{C}^{-\frac{1}{2}} S_i \bar{C}^{-\frac{1}{2}}) \bar{C}^{\frac{1}{2}} \quad (5)$$

To transport points $S_i \in \mathcal{T}_{\bar{C}} \mathcal{S}_D^+$ from the tangent space at \bar{C} to the tangent space at \bar{C}_ϕ , parallel transport on \mathcal{S}_D^+ can be used as:

$$\Gamma_{\bar{C} \rightarrow \bar{C}_\phi}(S_i) = P^\top S_i P, \quad P = (\bar{C}^{-1} \bar{C}_\phi)^{\frac{1}{2}} \quad (6)$$

While parallel transport is generally defined for tangent space vectors (Absil et al., 2008), for $(\mathcal{S}_D^+, g^{\text{AIRM}})$ it can be directly applied without explicitly computing tangent space projections (i.e., $\text{Exp}_{\bar{C}_\phi} \circ \Gamma_{\bar{C} \rightarrow \bar{C}_\phi} \circ \text{Log}_{\bar{C}} = \Gamma_{\bar{C} \rightarrow \bar{C}_\phi}$) (Brooks et al., 2019; Yair et al., 2019).

If \bar{C}_ϕ lies along the geodesic connecting \bar{C} with the identity matrix I_D , there exists a step-size $t \in \mathbb{R}$ so that $\bar{C}_\phi = \bar{C} \#_t I_D$, and (6) simplifies to Mellot et al. (2024):

$$\Gamma_{\bar{C} \rightarrow I_D}(C_i; t) = \Gamma_{\bar{C} \rightarrow \bar{C} \#_t I_D}(C_i) = \bar{C}^{-\frac{1}{2}} C_i \bar{C}^{-\frac{1}{2}} \quad (7)$$

3 METHODS

3.1 GENERATIVE MODEL

In the case of EEG, the features $x_i \in \mathcal{X} \subseteq \mathbb{R}^{P \times T}$ comprise epochs of multivariate time-series data with P spatial channels and T consecutive temporal samples. Propagation of brain activity to the EEG electrodes, located at the scalp, is typically modeled as a linear mixture of sources (Nunez & Srinivasan, 2006):

$$x_i := A_{j(i)} z_i \quad (8)$$

where $A_{j(i)} \in \{A \in \mathbb{R}^{P \times P} : \text{rank}(A)=P\}$ is a domain-specific forward model and $z_i \in \mathbb{R}^{P \times T}$ the activity of latent sources. Utilizing the uniqueness of the polar decomposition for invertible matrices, we constrain the model to

$$A_j := Q \exp(P_j) \quad (9)$$

where $Q \in \{Q \in \mathbb{R}^{P \times P} : Q^T Q = I_P\}$ is a orthogonal matrix modeling rotations and $\exp(P_j) \in \mathcal{S}_P^+$ a SPD matrix modeling domain-specific scalings.

Like (Sabbagh et al., 2020; Kobler et al., 2021; Mellot et al., 2024), we consider zero-mean (i.e., $\mathbb{E}\{z_i\} = 0_P \forall i$) signals, and a log-linear relationship between the spatial covariance $E_i = \text{Cov}(z_i) \in \mathcal{S}_P^+$ of the latent sources z_i and the target y_i . As graphically outlined in Figure 1a, we model the source covariance matrices as:

$$E_i := \exp \circ \text{upper}^{-1}(s_i) \quad (10)$$

where the linear mapping $\text{upper}^{-1} : \mathbb{R}^{P(P+1)/2} \rightarrow \mathcal{S}_P$ transforms a vector to a symmetric matrix while preserving its norm (i.e., $S \in \mathcal{S}_P : \|\text{upper}^{-1}(s)\|_F = \|s\|_2$), and latent log-space features $s_i \in \mathbb{R}^{P(P+1)/2}$ are generated as:

$$s_i := B \tilde{y}_i + \varepsilon_i, \quad \tilde{y}_i := 1_{y_i} - \pi_j \quad (11)$$

where 1_{y_i} represents one-hot-coded labels, $\pi_j = [p_j(y=y)]_{y=1, \dots, |\mathcal{Y}|}$ contains the class priors for domain j , $\varepsilon_i \in \mathbb{R}^{P(P+1)/2}$ is zero-mean additive noise, and $B \in \{B \in \mathbb{R}^{P(P+1)/2 \times |\mathcal{Y}|} : \text{rank}(B)=|\mathcal{Y}|\}$. We assume that the matrix B is sparse and structured so that label information in $\log(E_i)$ is only encoded in its first D -dimensional block (Figure 1a).

Proposition 1 *Given the specified generative model and a set of examples $\mathcal{E}_j = \{(E_i, y_i, j) | E_i \in \mathcal{S}_P^+, y_i \in \mathcal{Y}\}_{i \leq M_j}$ of domain $j \in \mathcal{J}$, we have that the Fréchet mean of \mathcal{E}_j , defined in (2), converges to the identity matrix I_P with $M_j \rightarrow \infty$ for all domains $j \in \mathcal{J}$.*

Our proof, provided in appendix A.1, relies on the uniqueness of the Fréchet mean for $(\mathcal{S}_P^+, g^{\text{AIRM}})$ and that \tilde{y}_i and ε_i in (11) are zero-mean.

For the generated multi-variate time-series features $x_i \in \mathcal{X}$ the empirical covariance matrix C_i is:

$$C_i := \text{Cov}(x_i) = \frac{1}{T} x_i x_i^T \in \mathcal{S}_P^+ \quad (12)$$

Due to the linear relationship between observed features and latent sources (8), we obtain a direct relationship to the latent source covariance matrices E_i :

$$C_i = A_{j(i)} E_i A_{j(i)}^T \quad (13)$$

Since E_i encodes the target $y_i \in \mathcal{Y}$ and A_j is invertible, C_i are sufficient descriptors to decode y_i .

Remark 1 *Note that for each domain j the covariance matrices of the generated data $\{C_i : j_i = j\}$ are not necessarily jointly diagonalizable. Depending on the structure of B and ε_i , the proposed generative model reduces to a jointly diagonalizable model if all the off-diagonal elements in $\log(E_i)$ are zero $\forall i$.*

3.2 DECODING FRAMEWORK

Given source domain data \mathcal{D}_s and a hypothesis class \mathcal{H} , we aim to learn a decoder function $h_s \in \mathcal{H}$, and - once the unlabeled target data \mathcal{D}_t is revealed - use \mathcal{D}_t and h_s to learn $h_t \in \mathcal{H}$. Following

Kobler et al. (2022a), we constrain the hypothesis class \mathcal{H} to functions $h : \mathcal{X} \times \mathcal{J} \rightarrow \mathcal{Y}$ that can be decomposed into a composition of a shared feature extractor $f_\theta : \mathcal{X} \rightarrow \mathcal{S}_D^+$, latent alignment $m_\phi : \mathcal{S}_D^+ \times \mathcal{J} \rightarrow \mathbb{R}^{D(D+1)/2}$, and a shared linear classifier $g_\psi : \mathbb{R}^{D(D+1)/2} \rightarrow \mathcal{Y}$ with parameters $\Theta = \{\theta, \phi, \psi\}$ (Figure 1b). Within this section, we focus on theoretical considerations for m_ϕ under our generative model.

Tangent space mapping (TSM) to recover $\log(E_i)$ Considering a set of labeled data $\mathcal{D} = \{(x_i, y_i) : x_i \in \mathcal{X}, y_i \in \mathcal{Y}, j_i = j \forall i\}$ obtained from a single domain j , TSM (Barachant et al., 2011) provides an established (Lotte et al., 2018; Jayaram & Barachant, 2018) decoding approach to infer y_i . TSM requires SPD-matrix valued representations. For the considered generative model, covariance features C_i , as defined in (12), are a natural choice (i.e., $f_\theta = \text{Cov}$). In a nutshell, TSM first estimates the Fréchet mean \bar{C} of $\mathcal{C} = \{\text{Cov}(x_i) : (x_i, y_i) \in \mathcal{D}\}$, projects each C_i to the tangent space at \bar{C} , and finally transports the data to vary around I_P . Formally,

$$\tilde{m}_\phi(C_i) := \text{upper} \circ \Gamma_{\bar{C} \rightarrow I} \circ \text{Log}_{\bar{C}}(C_i) = \text{upper} \left(\log \left(\bar{C}^{-\frac{1}{2}} C_i \bar{C}^{-\frac{1}{2}} \right) \right), \phi = \{\bar{C}\} \quad (14)$$

where the resulting representations of \tilde{m}_ϕ have a linear relationship to $\log(E_i)$ (Sabbagh et al., 2020; Kobler et al., 2021) and through (10) and (11) also to the labels y_i .

RCT+TSM compensates marginal and conditional shifts In the context of functional neuroimaging data, the recentering (RCT) transform (Zanini et al., 2017; Yair et al., 2019) and its extensions (Rodrigues et al., 2019; He & Wu, 2019; Kobler et al., 2022a; Mellot et al., 2023) address source-free UDA problems. Combined with TSM, RCT+TSM essentially applies (14) independently to each domain j . The outputs $\tilde{m}_{\phi(j(i))}(C_i)$, where $\phi(j) = \{\bar{C}_j\}$, are treated as domain-invariant and passed on to the shared classifier g_ψ .

Although RCT+TSM is an established method to address SFUDA problems for neuroimaging data (Lotte et al., 2018; Wei et al., 2022; Roy et al., 2022), there is a lack of understanding of what kind of distribution shifts RCT+TSM can compensate.

Proposition 2 *For the generative model, specified in section 3.1, RCT+TSM compensates conditional distribution shifts introduced by the invertible linear map A_j , defined in (8), and recovers domain-invariant representations if there are no label shifts (i.e., $p_j(y=y) = p(y=y) \forall y \in \mathcal{Y}, \forall j \in \mathcal{J}_s \cup \mathcal{J}_t$).*

A detailed proof is provided in appendix A.2. Starting with $\tilde{m}_{\phi(j(i))}(C_i)$, as defined in (14) and utilizing the unique polar decomposition (9) of A_j into rotational Q and scaling $\exp(P_j)$ transformations along with proposition 1 we obtain:

$$\log \left(\bar{C}_{j(i)}^{-\frac{1}{2}} C_i \bar{C}_{j(i)}^{-\frac{1}{2}} \right) = Q \log(E_i) Q^T = Q \text{upper}^{-1} (B (1_{y_i} - \pi_{j(i)}) + \varepsilon_i) Q^T \quad (15)$$

If there are no label shifts we have $\pi_j = \pi_k \forall j, k \in \mathcal{J}_s \cup \mathcal{J}_t$. Then (15) only contains domain-invariant terms on the right hand side. Thus, RCT+TSM compensates the conditional shifts introduced by $\exp(P_j)$. \square

Remark 2 *If all sources in (8) can be partitioned into relevant and irrelevant sources $z_i = [z_i^\parallel, z_i^\perp]$, $z_i^\parallel = f(y_i) \in \mathbb{R}^{D \times T}$, $z_i^\perp \neq f(y_i) \in \mathbb{R}^{(P-D) \times T}$ that are independent from each other, then the source covariance matrices E_i have a block-diagonal structure. Consequently, RCT+TSM compensates marginal shifts in z_i^\perp and conditional shifts in z_i^\parallel introduced by $\exp(P_j)$.*

Alignment under label shifts We aim to extend RCT+TSM to extract label shift invariant representations. Specifically, we aim to apply additional transformations on $(\mathcal{S}_D^+, g^{\text{ARM}})$ that attenuate the effect of class priors π_j in (15). We first rewrite (15) as:

$$\bar{C}_{j(i)}^{-\frac{1}{2}} C_i \bar{C}_{j(i)}^{-\frac{1}{2}} = \exp(Q \log(E_i) Q^T) = \exp(Q \text{upper}^{-1} (B (1_{y_i} - \pi_{j(i)}) + \varepsilon_i) Q^T) \quad (16)$$

$$= \exp \left(\underbrace{Q \text{upper}^{-1} (B 1_{y_i} + \varepsilon_i) Q^T}_{\log(\bar{E}_i)} - \underbrace{Q \text{upper}^{-1} (B \pi_{j(i)}) Q^T}_{\bar{P}_{j(i)}} \right) \quad (17)$$

where we split $\log(E_i)$ into domain-invariant $\log(\tilde{E}_i)$ and label shift $\bar{P}_{j(i)}$ terms. To separate both terms into products of matrices, we utilize $\exp(\alpha(A + B)) = \exp(\alpha B/2) \exp(\alpha A) \exp(\alpha B/2) + \mathcal{O}(\alpha^3)$ (Higham, 2008, Theorem 10.5), resulting in:

$$\bar{C}_{j(i)}^{-\frac{1}{2}} C_i \bar{C}_{j(i)}^{-\frac{1}{2}} = Q \exp(\bar{P}_{j(i)})^{-\frac{1}{2}} Q^T Q \tilde{E}_i Q^T Q \exp(\bar{P}_{j(i)})^{-\frac{1}{2}} Q^T + \mathcal{O}(\|\log(E_i)\|_F^3) \quad (18)$$

with the approximation error $\mathcal{O}(\|\log(E_i)\|_F^3)$ decaying cubically for $\|\log(E_i)\|_F < 1$. In this form, it is straightforward to see that an additional bilinear transformation on the left hand side in (18) with an SPD matrix can approximately compensate the effect of $\exp(\bar{P}_{j(i)})$. We denote this parameter as domain-specific bias parameter $\Phi_{j(i)} \in \mathcal{S}_D^+$, and generalize RCT+TSM to:

$$m_{\phi(j(i))}(C_i) = \text{upper} \circ \log \left(\Phi_{j(i)}^{\frac{1}{2}} \bar{C}_{j(i)}^{-\frac{1}{2}} C_i \bar{C}_{j(i)}^{-\frac{1}{2}} \Phi_{j(i)}^{\frac{1}{2}} \right), \quad \phi(j(i)) = \{\bar{C}_{j(i)}, \Phi_{j(i)}\} \quad (19)$$

Note that if $\exp(\bar{P}_j)$ and $\exp(P_j)$ share the same eigenvectors, they commute and lie on the same geodesic connecting $\exp(P_j)$ with I_D . Consequently, the combined effect of $\exp(\bar{P}_j)$ and $\exp(P_j)$ is constrained to the geodesic connecting \bar{C}_j with I_D . Then, the solution space can be constrained to $\Phi_j \in \{\Phi : \Phi \in \mathcal{S}_D^+, \Phi = \bar{C}_j \#_{\varphi_j} I_D, \varphi_j \in \mathbb{R}\}$, and (7) used to simplify (19) to:

$$m_{\phi(j(i))}^{\#}(C_i) = \text{upper} \circ \log \circ \Gamma_{\bar{C}_{j(i)} \rightarrow \bar{C}_{j(i)} \#_{\varphi_j(i)} I_D}(C_i), \quad \phi(j(i)) = \{\bar{C}_{j(i)}, \varphi_j(i)\} \quad (20)$$

where the geodesic step-size parameter $\varphi_j(i) \in \mathbb{R}$ needs to be learned.

Latent alignment with domain-specific SPD batch norm. Parametrizing the feature extractor $f_\theta : \mathcal{X} \rightarrow \mathcal{S}_D^+$ as a neural network naturally extends the decoding framework to neural networks with SPD matrix-valued features (Huang & Gool, 2017). In this end-to-end learning setting, SPD batch norm (SPDBN)(Brooks et al., 2019; Kobler et al., 2022b) and domain-specific batch norm (Kobler et al., 2022a) layers can be utilized to implement m_ϕ .

3.3 SPD MANIFOLD INFORMATION MAXIMIZATION

We utilize the labeled source domain dataset \mathcal{D}_s to learn the shared feature extractor f_θ , g_ψ , and m_ϕ for the source domains $j \in \mathcal{J}_s$ with the cross-entropy loss as the training objective (Figure 1b).

For the target domains, we keep f_θ and g_ψ fixed and learn $\phi(j) \forall j \in \mathcal{J}_t$ (Figure 1c). For each domain $j \in \mathcal{J}_t$, we use (2) to compute the Fréchet mean $\bar{C}_{j(i)}$ of $\mathcal{C}_j = \{f_\theta(x_i) : (x_i, j(i)) \in \mathcal{D}_t, j(i) = j\}$. To estimate $\Phi_{j(i)}$ in an unsupervised fashion, we employ the information maximization (IM) loss (Shi & Sha, 2012) to ensure that target outputs are individually certain and globally diverse. The IM loss is a popular training objective for SFUDA and test-time adaptation frameworks (Liang et al., 2020; 2024). In practice, when the target domain data is revealed, we initialize $\Phi_{j(i)}$ with I_D and $\varphi_j(i)$ with 1. We then minimize the following \mathcal{L}_{CEM} and \mathcal{L}_{MEM} that together constitute the \mathcal{L}_{IM} loss:

$$\begin{aligned} \mathcal{L}_{\text{IM}} &= \mathcal{L}_{\text{CEM}} + \mathcal{L}_{\text{MEM}} \quad (21) \\ \mathcal{L}_{\text{CEM}} &= -\mathbb{E}_{(x_i, j_i) \in \mathcal{D}_t} \left\{ \sum_{k=1}^{|\mathcal{Y}|} \delta_k \left(\frac{h_t(x_i, j_i)}{T} \right) \log \delta_k \left(\frac{h_t(x_i, j_i)}{T} \right) \right\} \\ \mathcal{L}_{\text{MEM}} &= \sum_{k=1}^{|\mathcal{Y}|} \hat{p}_k \log \hat{p}_k, \quad \hat{p}_k = \mathbb{E}_{(x_i, j_i) \in \mathcal{D}_t} \left\{ \delta_k \left(\frac{h_t(x_i, j_i)}{T} \right) \right\} \end{aligned}$$

where δ_k is the k-th element of the softmax output, \mathcal{L}_{CEM} is conditional entropy minimization, \mathcal{L}_{MEM} is marginal entropy maximization and factor T is temperature scaling. IM balance is more effective than conditional entropy minimization because minimizing only the conditional entropy may lead to model collapse with all test data allocated to one class (Grandvalet & Bengio, 2004). We additionally employed a temperature scaling factor T to adjust the model's prediction confidence on the target data, a common technique for calibrating probabilistic models (Li et al., 2023; Guo et al., 2017). Temperature scaling uses a single scalar parameter $T > 0$ for all classes, and it increases the softmax output entropy when $T > 1$ and decreases it when $0 < T < 1$.

4 EXPERIMENTS

We conducted simulations and experiments with public EEG motor imagery and sleep stage datasets to evaluate our proposed framework empirically.

Multi-source domain training Following Kobler et al. (2022a), we parameterize $h_s = g_\psi \circ m_\phi \circ f_\theta$ as a neural network and fit the source decoder h_s in an end-to-end fashion (Figure 1b), denoted as TSMNet. We used the standard-cross entropy loss as training objective, and optimized the parameters with the Riemannian ADAM optimizer (Bécigneul & Ganea, 2018). We split the source domains’ data into training and validation sets (80% / 20% splits, randomized, stratified by domain and label) and iterated through the training set for 100 epochs. We stick to the TSMNet hyper-parameters as provided in the public reference implementation (for implementation details see Appendix A.7.1).

SPDIM Source-free domain adaptation SPDIM keeps the fitted source feature extractor f_θ and linear classifier g_ψ fixed and estimates a domain-specific bias parameter for latent alignment m_ϕ (Figure 1c). Depending on the choice of the bias parameter, we distinguish between SPDIM(bias), defined in (19), and SPDIM(geodesic), defined in (20). We use the entire target domain data to estimate gradients for the IM loss (21) and Riemannian ADAM to optimize the bias parameter for 50 epochs.

SFUDA Baseline Methods. We consider several multi-source (-target) SFUDA baseline methods, including Recenter (RCT) (Zanini et al., 2017), Euclidean alignment (EA) (He & Wu, 2019), and spatio-temporal Monge alignment (STMA) (Gnassounou et al., 2024). These alignment methods are model-agnostic techniques that are applied to the EEG data before a classifier is fitted. Among the end-to-end learning SFUDA methods, we consider SPDDSBN (Kobler et al., 2022a) which was introduced together with the TSMNet architecture. Lastly, we compare SPDIM to classic IM approaches (Shi & Sha, 2012) that adapt parameters in f_θ or g_ψ .

No DA Baseline Methods. Methods in this category, denoted w/o SFUDA, treat the problem as a standard supervised learning problem; they do not utilize the domain labels $\mathcal{J}_s \cup \mathcal{J}_t$ during training and testing. In models that perform TSM, all data are projected to the tangent space at the Fréchet mean of the entire source dataset \mathcal{D}_s .

We used publicly available Python code for baseline methods and implemented custom methods using the packages torch (Paszke et al., 2019), scikit-learn (Pedregosa et al., 2011), braindecode (Schirrmester et al., 2017), geoopt (Kochurov et al., 2020) and pyRiemann Barachant et al. (2023). We conducted the experiments on standard computation PCs with 32-core CPUs, 128 GB of RAM, and a single GPU.

4.1 SIMULATIONS

To examine the effectiveness of SPDIM, we simulated binary classification problems under our generative model (implementation details in Appendix A.6). We used balanced accuracy as evaluation metric and examined the performance of SPDIM(bias) and SPDIM(geodesic) against RCT (Zanini et al., 2017) over different label ratios. Figure 2 summarizes the results for different class separability levels. Supplementary Figures display the methods’ performance over parameters $|\mathcal{J}_s|$ (Figure A1), M_j (Figure A2), P (Figure A3), and D (Figure A4).

The simulation results empirically confirm Proposition 2. That is, RCT can compensate the conditional shifts introduced by A_j if there are no labels shifts (i.e., label ratio = 1.0). They also demonstrate that as the label shifts become more severe (i.e., lower label ratio), the average performance of SPDIM decreases while the variability increases. Still, SPDIM outperforms RCT across almost all considered parameter configurations.

4.2 EEG MOTOR IMAGERY DATA

Almost all public motor imagery datasets are generated in a highly controlled lab environment and designed to be balanced. However, in realistic brain-computer interface application settings, the variability of human behavior and environmental factors likely cause label shifts across days and subjects. To bridge the gap between controlled research settings and real-world scenarios, we artificially introduced label shifts in the target domains.

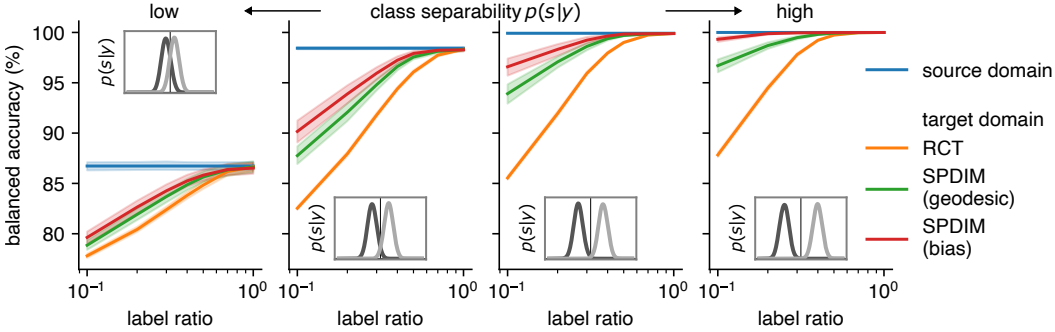


Figure 2: **Simulation results.** Balanced accuracy scores (higher is better) across target domain label ratios (i.e., majority to minority label ratio) on the x-axis and class separability $p(s|y)$ across panels. Source domain labels were balanced.

We considered 4 public motor imagery datasets: BNCI2014001 (Tangermann et al., 2012) (9 subjects/2 sessions/4 classes/22 channels), BNCI2015001 (Faller et al., 2012) (12/2-3/2/13), Zhou2016 (Zhou et al., 2016) (4/3/3/14), and BNCI2014004 (Leeb et al., 2007) (9/5/2/3). We used MOABB (Jayaram & Barachant, 2018; Chevallier et al., 2024) to pre-process the continuous time-series data and extract labeled epochs. Pre-processing included resampling EEG signals to 250 or 256 Hz, applying temporal filters to capture frequencies between 4 and 36 Hz, and extracting 3-second epochs linked to specific class labels. Following Kobler et al. (2022a), we use TSMNet as model architecture and treat sessions as domains, and use a leave-one-group-out cross-validation (CV) scheme to fit and evaluate the methods. To evaluate cross-session transfer, we fitted and evaluated models independently per subject and treated the session as the grouping variable. To evaluate cross-subject transfer, we treated the subject as the grouping variable. After running pilot experiments with the BNCI2014001 dataset, we set the temperature scaling factor in (21) to $T = 2$ for binary classification problems and $T = 0.8$ otherwise. Early stopping were fit with a single stratified (domain and labels) inner train/validation split. We used balanced accuracy as the metric to examine the performance of each method at label ratios of 1.0 and 0.2 for the source and target domains, respectively.

Grand average results across all 4 datasets are summarized in Figure 3, and grouped by the transfer learning scenario (cross-session, cross-subject). To attenuate large variability across subjects, we report scores relative to the score obtained with SPDDSBN w/o label shifts (i.e., 1.0 label ratio). Detailed results per dataset are listed in Table A4 (w/ label shifts) and Table A4 (w/o label shifts) along with the ones of relevant baseline methods. Although no method can perfectly compensate the artificially introduced label shifts, SPDIM(bias) is consistently at the top (cross-subject) or among the top (cross-session) performing methods. Significance testing ($n=34$ subjects), summarized in Table A4, revealed that the performance of SPDIM(bias) is significantly higher than w/o, SPDDSBN, IM(classifier), and IM(all) in the cross-subject setting as well as SPDDSBN, IM(classifier), and IM(all) in the cross-session scenario.

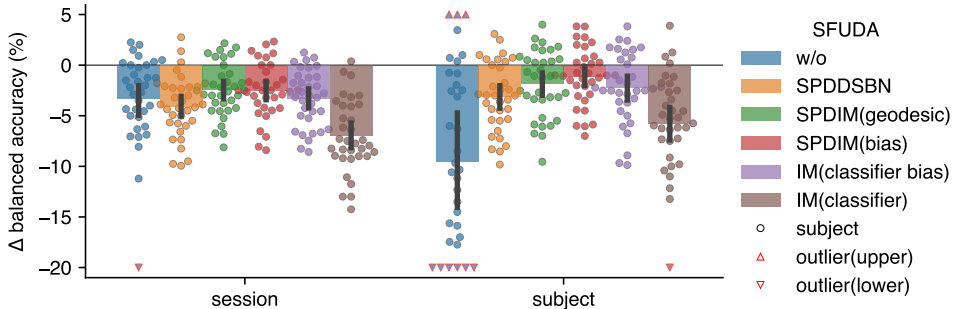


Figure 3: **Motor-imagery results (0.2 label ratio).** Average of test-set scores (balanced accuracy; higher is better; error bars indicate 95% confidence interval) relative to TSMNet+SPDDSBN (Kobler et al., 2022a) w/o label shifts. For extended results per dataset, see Tables A4 and A5.

4.3 EEG-BASED SLEEP STAGING

The aim of this experiment is to demonstrate the effectiveness of our method on datasets with inherent label shifts. Due to the inherent variability of sleep, most sleep stage datasets exhibit label shifts across subjects (Eldele et al., 2023). Sleep stage classification plays a key role in assessing sleep quality and diagnosing sleep disorders (Perez-Pozuelo et al., 2020). Yet, automated frameworks lack accuracy and suffer from poor generalization across domains, resulting in accuracy drops compared to expert neurologists.

We considered 4 public sleep stage datasets: CAP (Terzano et al., 2001; Goldberger et al., 2000), Dreem (Guillot et al., 2020), HMC (Alvarez-Estevéz & Rijsman, 2021a;b), and ISRUC (Khalighi et al., 2016). A detailed description is provided in Supplementary Table A1. We consider sleep stages following the AASM (Berry et al., 2012) standard (W, N1, N2, N3, REM). If data was originally scored following the K&M (Wolpert, 1969) standard (W, S1, S2, S3, S4, REM), we merged stages S3 and S4 into a single stage N3. EEG data pre-processing followed (Guillot & Thorey, 2021) and was implemented with MNE-python (Gramfort et al., 2014). First, all EEG channels were retained, and an IIR band-pass filter ranging from 0.2 to 30 Hz was applied. The signals were then resampled to 100 Hz, and non-overlapping 30-second epochs were extracted together with the associated labels. To attenuate the effects of gross outliers, each recording was scaled to have unit inter-quartile range and a median of zero, and values exceeding 20 times the inter-quartile range were clipped Perslev et al. (2021). Lastly, subjects with corrupted data (e.g., mismatched labels and epochs) were excluded, resulting in a total of 426 remaining subjects.

Since label shifts occur in the source domains of sleep stage data, the considered models are trained with a balanced mini-batch sampler, which is a popular method to compensate for label shifts during training in deep learning (Cao et al., 2019). The balanced sampler over-sampled minority classes to ensure that the label distribution per domain is balanced within each mini-batch.

To evaluate the methods, we employed a 10-fold grouped cross-validation scheme, ensuring that each group (i.e., subject) appears either in the training set (i.e., source domains) or the test set (i.e., target domains). As before, we set the temperature scaling factor $T = 0.8$ and used stratified (labels and domains) inner train/validation splits for early stopping. In addition to the TSMNet architecture, we included four baseline deep learning architectures specifically proposed for sleep staging: Chambon (Chambon et al., 2018), Usleep (Perslev et al., 2021), DeepSleepNet (Supratak et al., 2017), and AttnNet (Eldele et al., 2023) (implementation details in Appendix A.7.2).

Table 1 summarizes the results across datasets along with the grand average results of published baseline methods. Extended results for all considered baseline methods are listed in Supplementary Table A2. TSMNet+SPDIM(bias) significantly outperforms all other methods for the patient and healthy (except TSMNet+STMA) subject groups. Overall, the margin to TSMNet+SPDDBN was approx. 5% in the patient group, which indicates that SPDIM has great potential for clinical applications.

Ablation Study Table 2 summarizes grand average test scores relative to SPDIM(bias). We highlight four observations. First, all considered ablations lead to a significant performance drop of at least 3% compared to SPDIM(bias), suggesting the combined importance of IM paired with the manifold-constrained bias parameter. Second, in the presence of label shifts, fitting \tilde{m}_ϕ per domain (i.e., TSMNet+SPDDBN) hurts generalization compared to global \tilde{m}_ϕ (i.e., TSMNet+w/o). Third, fine-tuning the classifier bias parameter yields approximately the same performance as SPDIM(geodesic), extending the finding of (Mellot et al., 2024) from regression to classification scenarios. Fourth, IM methods obtained the top 3 scores, but two variants failed to improve upon the global method, which underscores the importance of regularization (i.e., via selecting the right parameter) to prevent the IM loss from overfitting.

5 DISCUSSION

We proposed a geometric deep learning framework, denoted SPDIM, to address SFUDA problems with conditional and label shifts and demonstrated its utility in highly relevant EEG-based neurotechnology application scenarios. We first introduced a realistic generative model, and provided theoretical analyses showing that prior Riemannian statistical alignment methods that align

Model	Dataset:	CAP		Dreem		HMC	ISRUC		Overall	
	Group: SFUDA	patient (n=82)	healthy (n=22)	patient (n=50)	patient (n=154)	healthy (n=10)	patient (n=108)	healthy (n=32)	patient (n=394)	
Chambon	w/o	• 64.7 (10.7)	• 65.2 (9.1)	• 53.4 (16.2)	• 64.0 (9.6)	72.7 (3.9)	• 68.9 (8.2)	• 67.5 (8.6)	• 64.2 (11.5)	
	EA	• 63.8 (11.3)	• 64.7 (10.3)	• 54.5 (14.4)	• 63.4 (10.7)	74.9 (4.8)	70.7 (9.3)	• 67.9 (10.0)	• 64.3 (12.0)	
	STMA	• 65.2 (10.0)	• 67.1 (7.7)	• 51.3 (19.0)	• 63.8 (9.1)	74.8 (4.4)	70.8 (7.6)	• 69.5 (7.7)	• 64.4 (12.1)	
USleep	w/o	• 59.1 (10.3)	• 55.9 (8.3)	• 48.4 (8.2)	• 66.6 (9.3)	72.9 (6.1)	• 68.8 (8.3)	• 61.3 (11.0)	• 63.3 (11.3)	
Deep-SleepNet	w/o	• 68.1 (11.3)	• 68.6 (9.9)	68.7 (10.3)	• 64.9 (10.3)	75.8 (4.5)	72.7 (9.1)	70.9 (9.1)	• 68.2 (10.7)	
AttnSleep	w/o	68.9 (10.3)	• 65.4 (10.7)	• 61.7 (14.2)	67.7 (10.0)	75.4 (4.0)	73.1 (8.6)	• 68.5 (10.2)	68.7 (10.9)	
TSMNet	w/o	• 68.0 (11.2)	• 65.9 (9.6)	66.7 (12.4)	• 63.6 (11.3)	• 73.4 (3.9)	• 68.7 (9.3)	• 68.3 (8.9)	• 66.3 (11.1)	
	SPDDSBN	• 68.2 (8.8)	• 68.9 (5.8)	• 64.2 (8.5)	• 62.2 (6.0)	• 72.8 (2.8)	• 66.6 (6.4)	• 70.1 (5.3)	• 64.9 (7.5)	
	SPDIM(bias) (proposed)	71.0 (9.6)	72.1 (8.0)	68.1 (9.8)	68.6 (8.5)	76.7 (3.4)	71.6 (6.9)	73.5 (7.2)	69.9 (8.6)	

Table 1: **Sleep-staging results per dataset.** Average of test-set scores (balanced accuracy; higher is better; standard-deviation in brackets). Permutation-paired t-tests were used to identify significant differences between TSMNet+SPDIM (*proposed*) and baseline methods (1e4 permutations, 14 tests, t-max correction). Significant differences are highlighted ($\bullet p \leq 0.05$, $\circ p \leq 0.01$, $\bullet p \leq 0.001$). Extended results are provided in Table A2.

Alignment	fit Fréchet mean	\mathcal{L}_{IM}	Θ_{IM}	mean (std)	t-val (p-val)
m_ϕ (19)	per domain j	✓	Φ_j	-	-
$m_\phi^\#$ (20)	per domain j	✓	φ_j	-3.0 (3.6)	-17.4 (0.0001)
\tilde{m}_ϕ (14)	per domain j	✗	-	-4.8 (4.5)	-22.1 (0.0001)
\tilde{m}_ϕ (14)	global (i.e., \mathcal{D}_s)	✗	-	-3.7 (8.5)	-9.0 (0.0001)
\tilde{m}_ϕ (14)	per domain j	✓	bias in ψ	-3.0 (3.8)	-16.1 (0.0001)
\tilde{m}_ϕ (14)	per domain j	✓	ψ	-4.8 (5.4)	-18.5 (0.0001)
\tilde{m}_ϕ (14)	per domain j	✓	$\theta \cup \psi$	-27.1 (13.5)	-41.5 (0.0001)

Table 2: **Sleep-staging ablation results.** Balanced accuracy scores (higher is better) relative to the proposed method. Averages and standard deviation summarize the individual (n=426 subjects) test-set scores. Student’s t values and adjusted p values indicate the effect strength (permutation-paired t-tests, 1e4 permutations, 6 tests, t-max correction). Table A3 lists results per dataset and group.

the Fréchet mean can compensate for the conditional distribution shifts introduced in our generative model, but hurt generalization under additional label shifts. As a remedy, we proposed SPDIM to learn a domain-specific SPD manifold-constrained bias parameter to compensate for over-corrections introduced via aligning the Fréchet means by employing the information maximization principle. In simulations and experiments with real EEG data, SPDIM consistently achieved the highest scores among the considered baseline methods.

A limitation of our framework is that the IM loss, due to large noise and outliers, can sometimes estimate an inappropriate bias parameter, leading to the data being shifted in the wrong direction. While it generally improves average performance, it also increases variability. We expect future work to explore a more robust way to estimate the bias parameter.

6 ACKNOWLEDGMENTS

Motoaki Kawanabe and Reinmar J Kobler were partially supported by the Innovative Science and Technology Initiative for Security Grant Number JPJ004596, ATLA and KAKENHI (Grants-in-Aid for Scientific Research) under Grant Numbers 21K12055, JSPS, Japan.

7 AUTHOR CONTRIBUTIONS

Shanglin Li contributed to the study under the co-supervision of Motoaki Kawanabe and Reinmar J. Kobler. Shanglin Li and Reinmar J. Kobler developed the decoding methods. Reinmar J. Kobler contributed the theoretical analysis. Shanglin Li and Reinmar J. Kobler performed the simulation experiments. Shanglin Li conducted the experiments with EEG data. The draft of the manuscript was written by Shanglin Li and Reinmar Kobler. All authors read and approved the final manuscript.

REFERENCES

- P-A Absil, Robert Mahony, and Rodolphe Sepulchre. *Optimization algorithms on matrix manifolds*. Princeton University Press, 2008.
- Dinesh Acharya, Zhiwu Huang, Danda Pani Paudel, and Luc Van Gool. Covariance pooling for facial expression recognition. In *Proceedings of the IEEE conference on computer vision and pattern recognition workshops*, pp. 367–374, 2018.
- Turkey N Alotaiby, Saleh A Alshebeili, Tariq Alshawi, Ishtiaq Ahmad, and Fathi E Abd El-Samie. Eeg seizure detection and prediction algorithms: a survey. *EURASIP Journal on Advances in Signal Processing*, 2014:1–21, 2014. doi: 10.1186/1687-6180-2014-183.
- Diego Alvarez-Estevéz and RM Rijsman. Haaglanden medisch centrum sleep staging database (version 1.0. 1). *PhysioNet*, 2021a. doi: 10.13026/t79q-fr32.
- Diego Alvarez-Estevéz and Roselyne M Rijsman. Inter-database validation of a deep learning approach for automatic sleep scoring. *PloS one*, 16(8):e0256111, 2021b. doi: 10.1371/journal.pone.0256111.
- Stylios Bakas, Siegfried Ludwig, Dimitrios A Adamos, Nikolaos Laskaris, Yannis Panagakis, and Stefanos Zafeiriou. Latent alignment with deep set eeg decoders. *arXiv preprint arXiv:2311.17968*, 2023.
- Alexandre Barachant, Stéphane Bonnet, Marco Congedo, and Christian Jutten. Multiclass brain-computer interface classification by riemannian geometry. *IEEE Transactions on Biomedical Engineering*, 59(4):920–928, 2011. doi: 10.1109/TBME.2011.2172210.
- Alexandre Barachant, Quentin Barthélemy, Jean-Rémi King, Alexandre Gramfort, Sylvain Chevalier, Pedro L. C. Rodrigues, Emanuele Olivetti, Vladislav Goncharenko, Gabriel Wagner vom Berg, Ghiles Reguig, Arthur Lebeurrier, Erik Bjäreholt, Maria Sayu Yamamoto, Pierre Clisson, and Marie-Constance Corsi. pyriemann/pyriemann: v0.5, 2023. URL <https://doi.org/10.5281/zenodo.8059038>.
- Gary Bécigneul and Octavian-Eugen Ganea. Riemannian adaptive optimization methods. *arXiv preprint arXiv:1810.00760*, 2018.
- Shai Ben-David, John Blitzer, Koby Crammer, Alex Kulesza, Fernando Pereira, and Jennifer Wortman Vaughan. A theory of learning from different domains. *Machine learning*, 79:151–175, 2010. doi: 10.1007/s10994-009-5152-4.
- Richard B Berry, Rohit Budhiraja, Daniel J Gottlieb, David Gozal, Conrad Iber, Vishesh K Kapur, Carole L Marcus, Reena Mehra, Sairam Parthasarathy, Stuart F Quan, et al. Rules for scoring respiratory events in sleep: update of the 2007 aasm manual for the scoring of sleep and associated events: deliberations of the sleep apnea definitions task force of the american academy of sleep medicine. *Journal of clinical sleep medicine*, 8(5):597–619, 2012. doi: 10.5664/jcsm.2172.

- Rajendra Bhatia. *Positive definite matrices*. Princeton university press, 2009. ISBN 978-0-691-12918-1.
- Rajendra Bhatia. The Riemannian Mean of Positive Matrices. In Frank Nielsen and Rajendra Bhatia (eds.), *Matrix Information Geometry*, pp. 35–51. Springer Berlin Heidelberg, Berlin, Heidelberg, 2013. ISBN 978-3-642-30232-9. doi: 10.1007/978-3-642-30232-9_2.
- Daniel Brooks, Olivier Schwander, Frédéric Barbaresco, Jean-Yves Schneider, and Matthieu Cord. Riemannian batch normalization for spd neural networks. *Advances in Neural Information Processing Systems*, 32, 2019.
- Kaidi Cao, Colin Wei, Adrien Gaidon, Nikos Arechiga, and Tengyu Ma. Learning imbalanced datasets with label-distribution-aware margin loss. *Advances in neural information processing systems*, 32, 2019.
- Stanislas Chambon, Mathieu N Galtier, Pierrick J Arnal, Gilles Wainrib, and Alexandre Gramfort. A deep learning architecture for temporal sleep stage classification using multivariate and multi-modal time series. *IEEE Transactions on Neural Systems and Rehabilitation Engineering*, 26(4): 758–769, 2018. doi: 10.1109/TNSRE.2018.2813138.
- Sylvain Chevallier, Igor Carrara, Bruno Aristimunha, Pierre Guetschel, Sara Sedlar, Bruna Lopes, Sebastien Velut, Salim Khazem, and Thomas Moreau. The largest EEG-based BCI reproducibility study for open science: the MOABB benchmark, April 2024. URL <http://arxiv.org/abs/2404.15319>.
- Antoine Collas, Rémi Flamary, and Alexandre Gramfort. Weakly supervised covariance matrices alignment through stiefel matrices estimation for meg applications. *arXiv preprint arXiv:2402.03345*, 2024.
- Marco Congedo, Alexandre Barachant, and Rajendra Bhatia. Riemannian geometry for eeg-based brain-computer interfaces; a primer and a review. *Brain-Computer Interfaces*, 4(3):155–174, 2017. doi: 10.1080/2326263X.2017.1297192.
- Emadeldeen Eldele, Mohamed Ragab, Zhenghua Chen, Min Wu, Chee-Keong Kwoh, and Xiaoli Li. Self-supervised learning for label-efficient sleep stage classification: A comprehensive evaluation. *IEEE Transactions on Neural Systems and Rehabilitation Engineering*, 31:1333–1342, 2023. doi: 10.1109/TNSRE.2023.3245285.
- Stephen H Fairclough and Fabien Lotte. Grand challenges in neurotechnology and system neuroergonomics. *Frontiers in Neuroergonomics*, 1:602504, 2020. doi: 10.3389/fnrgo.2020.602504.
- Josef Faller, Carmen Vidaurre, Teodoro Solis-Escalante, Christa Neuper, and Reinhold Scherer. Autocalibration and recurrent adaptation: Towards a plug and play online erd-bci. *IEEE Transactions on Neural Systems and Rehabilitation Engineering*, 20(3):313–319, 2012. doi: 10.1109/TNSRE.2012.2189584.
- Théo Gnassounou, Antoine Collas, Rémi Flamary, Karim Lounici, and Alexandre Gramfort. Multi-source and test-time domain adaptation on multivariate signals using spatio-temporal monge alignment. *arXiv preprint arXiv:2407.14303*, 2024.
- Ary L Goldberger, Luis AN Amaral, Leon Glass, Jeffrey M Hausdorff, Plamen Ch Ivanov, Roger G Mark, Joseph E Mietus, George B Moody, Chung-Kang Peng, and H Eugene Stanley. Physiobank, physiotoolkit, and physionet: components of a new research resource for complex physiologic signals. *circulation*, 101(23):e215–e220, 2000. doi: 10.1161/01.cir.101.23.e215.
- Alexandre Gramfort, Martin Luessi, Eric Larson, Denis A Engemann, Daniel Strohmeier, Christian Brodbeck, Lauri Parkkonen, and Matti S Hämäläinen. Mne software for processing meg and eeg data. *neuroimage*, 86:446–460, 2014. doi: 10.1016/j.neuroimage.2013.10.027.
- Yves Grandvalet and Yoshua Bengio. Semi-supervised learning by entropy minimization. *Advances in neural information processing systems*, 17, 2004.

- Antoine Guillot and Valentin Thorey. Robustsleepnet: Transfer learning for automated sleep staging at scale. *IEEE Transactions on Neural Systems and Rehabilitation Engineering*, 29:1441–1451, 2021. doi: 10.1109/TNSRE.2021.3098968.
- Antoine Guillot, Fabien Sauvet, Emmanuel H During, and Valentin Thorey. Dreem open datasets: Multi-scored sleep datasets to compare human and automated sleep staging. *IEEE transactions on neural systems and rehabilitation engineering*, 28(9):1955–1965, 2020. doi: 10.1109/TNSRE.2020.3011181.
- Chuan Guo, Geoff Pleiss, Yu Sun, and Kilian Q Weinberger. On calibration of modern neural networks. In *International conference on machine learning*, pp. 1321–1330. PMLR, 2017.
- He He and Dongrui Wu. Transfer learning for brain–computer interfaces: A euclidean space data alignment approach. *IEEE Transactions on Biomedical Engineering*, 67(2):399–410, 2019. doi: 10.1109/TBME.2019.2913914.
- Nicholas J. Higham. *Functions of Matrices: Theory and Computation*. Society for Industrial and Applied Mathematics, January 2008. ISBN 978-0-89871-646-7 978-0-89871-777-8. doi: 10.1137/1.9780898717778. URL <http://epubs.siam.org/doi/book/10.1137/1.9780898717778>.
- Judy Hoffman, Mehryar Mohri, and Ningshan Zhang. Algorithms and theory for multiple-source adaptation. *Advances in neural information processing systems*, 31, 2018.
- Zhiwu Huang and Luc Van Gool. A Riemannian Network for SPD Matrix Learning. In *Proceedings of the Thirty-First AAAI Conference on Artificial Intelligence, AAAI’17*, pp. 2036–2042. AAAI Press, 2017.
- Catalin Ionescu, Orestis Vantzos, and Cristian Sminchisescu. Matrix backpropagation for deep networks with structured layers. In *Proceedings of the IEEE international conference on computer vision*, pp. 2965–2973, 2015.
- Vinay Jayaram and Alexandre Barachant. Moabb: trustworthy algorithm benchmarking for bcis. *Journal of neural engineering*, 15(6):066011, 2018. doi: 10.1088/1741-2552/aadea0.
- Xiaopeng Ji, Yan Li, and Peng Wen. 3dsleepnet: A multi-channel bio-signal based sleep stages classification method using deep learning. *IEEE Transactions on Neural Systems and Rehabilitation Engineering*, 2023.
- Ce Ju and Cuntai Guan. Deep Optimal Transport on SPD Manifolds for Domain Adaptation. *arXiv*, 2201.05745, 2022.
- Sirvan Khalighi, Teresa Sousa, José Moutinho Santos, and Urbano Nunes. Isruc-sleep: A comprehensive public dataset for sleep researchers. *Computer methods and programs in biomedicine*, 124:180–192, 2016. doi: 10.1016/j.cmpb.2015.10.013.
- Reinmar Kobler, Jun-ichiro Hirayama, Qibin Zhao, and Motoaki Kawanabe. Spd domain-specific batch normalization to crack interpretable unsupervised domain adaptation in eeg. *Advances in Neural Information Processing Systems*, 35:6219–6235, 2022a.
- Reinmar J Kobler, Jun-Ichiro Hirayama, Lea Hehenberger, Catarina Lopes-Dias, Gernot R Müller-Putz, and Motoaki Kawanabe. On the interpretation of linear riemannian tangent space model parameters in m/eeg. In *2021 43rd Annual International Conference of the IEEE Engineering in Medicine & Biology Society (EMBC)*, pp. 5909–5913. IEEE, 2021.
- Reinmar J. Kobler, Jun-ichiro Hirayama, and Motoaki Kawanabe. Controlling The Fréchet Variance Improves Batch Normalization on the Symmetric Positive Definite Manifold. In *ICASSP 2022 - 2022 IEEE International Conference on Acoustics, Speech and Signal Processing (ICASSP)*, pp. 3863–3867, Singapore, Singapore, 2022b. IEEE. doi: 10.1109/ICASSP43922.2022.9746629.
- Max Kochurov, Rasul Karimov, and Serge Kozlukov. Geopt: Riemannian optimization in pytorch. *arXiv preprint arXiv:2005.02819*, 2020.

- Robert Leeb, Felix Lee, Claudia Keinrath, Reinhold Scherer, Horst Bischof, and Gert Pfurtscheller. Brain–computer communication: motivation, aim, and impact of exploring a virtual apartment. *IEEE Transactions on Neural Systems and Rehabilitation Engineering*, 15(4):473–482, 2007. doi: 10.1109/TNSRE.2007.906956.
- Siyang Li, Ziwei Wang, Hanbin Luo, Lieyun Ding, and Dongrui Wu. T-time: Test-time information maximization ensemble for plug-and-play bcis. *IEEE Transactions on Biomedical Engineering*, 2023. doi: 10.1109/TBME.2023.3303289.
- Xinhao Li, Jingjing Li, Lei Zhu, Guoqing Wang, and Zi Huang. Imbalanced source-free domain adaptation. In *Proceedings of the 29th ACM international conference on multimedia*, pp. 3330–3339, 2021.
- Jian Liang, Dapeng Hu, and Jiashi Feng. Do we really need to access the source data? source hypothesis transfer for unsupervised domain adaptation. In *International conference on machine learning*, pp. 6028–6039. PMLR, 2020.
- Jian Liang, Ran He, and Tieniu Tan. A Comprehensive Survey on Test-Time Adaptation Under Distribution Shifts. *International Journal of Computer Vision*, July 2024. doi: 10.1007/s11263-024-02181-w.
- Yuang Liu, Wei Zhang, and Jun Wang. Source-free domain adaptation for semantic segmentation. In *Proceedings of the IEEE/CVF Conference on Computer Vision and Pattern Recognition*, pp. 1215–1224, 2021.
- Fabien Lotte, Laurent Bougrain, Andrzej Cichocki, Maureen Clerc, Marco Congedo, Alain Rakotomamonjy, and Florian Yger. A review of classification algorithms for eeg-based brain–computer interfaces: a 10 year update. *Journal of neural engineering*, 15(3):031005, 2018. doi: 10.1088/1741-2552/aab2f2.
- Jingying Ma, Qika Lin, Ziyu Jia, and Mengling Feng. St-usleepnet: A spatial-temporal coupling prominence network for multi-channel sleep staging. *arXiv preprint arXiv:2408.11884*, 2024.
- Apolline Mellot, Antoine Collas, Pedro LC Rodrigues, Denis Engemann, and Alexandre Gramfort. Harmonizing and aligning m/eeg datasets with covariance-based techniques to enhance predictive regression modeling. *Imaging Neuroscience*, 1:1–23, 2023. doi: 10.1162/imag_a_00040.
- Apolline Mellot, Antoine Collas, Sylvain Chevallier, Alexandre Gramfort, and Denis A Engemann. Geodesic optimization for predictive shift adaptation on eeg data. *arXiv preprint arXiv:2407.03878*, 2024.
- Maher Moakher. A Differential Geometric Approach to the Geometric Mean of Symmetric Positive-Definite Matrices. *SIAM Journal on Matrix Analysis and Applications*, 26(3):735–747, 2005. doi: 10.1137/S0895479803436937.
- Ernst Niedermeyer and FH Lopes da Silva. *Electroencephalography: basic principles, clinical applications, and related fields*. Lippincott Williams & Wilkins, 2005. ISBN 978-0190228484.
- Paul L Nunez and Ramesh Srinivasan. *Electric fields of the brain: the neurophysics of EEG*. Oxford University Press, USA, 2006. ISBN 9780195050387.
- Adam Paszke, Sam Gross, Francisco Massa, Adam Lerer, James Bradbury, Gregory Chanan, Trevor Killeen, Zeming Lin, Natalia Gimelshein, Luca Antiga, et al. Pytorch: An imperative style, high-performance deep learning library. *Advances in neural information processing systems*, 32, 2019.
- Fabian Pedregosa, Gaël Varoquaux, Alexandre Gramfort, Vincent Michel, Bertrand Thirion, Olivier Grisel, Mathieu Blondel, Peter Prettenhofer, Ron Weiss, Vincent Dubourg, et al. Scikit-learn: Machine learning in python. *the Journal of machine Learning research*, 12:2825–2830, 2011. doi: 10.5555/1953048.2078195.
- Xavier Pennec. Barycentric subspace analysis on manifolds. *The Annals of Statistics*, 46, 2018. doi: 10.1214/17-AOS1636.

- Ignacio Perez-Pozuelo, Bing Zhai, Joao Palotti, Raghvendra Mall, Michaël Aupetit, Juan M Garcia-Gomez, Shahrad Taheri, Yu Guan, and Luis Fernandez-Luque. The future of sleep health: a data-driven revolution in sleep science and medicine. *NPJ digital medicine*, 3(1):42, 2020. doi: 10.1038/s41746-020-0244-4.
- Mathias Perslev, Sune Darkner, Lykke Kempfner, Miki Nikolic, Poul Jørgen Jennum, and Christian Igel. U-sleep: resilient high-frequency sleep staging. *NPJ digital medicine*, 4(1):72, 2021. doi: 10.1038/s41746-021-00440-5.
- Gert Pfurtscheller and FH Lopes Da Silva. Event-related eeg/meg synchronization and desynchronization: basic principles. *Clinical neurophysiology*, 110(11):1842–1857, 1999. doi: 10.1016/s1388-2457(99)00141-8.
- Pedro Luiz Coelho Rodrigues, Christian Jutten, and Marco Congedo. Riemannian Procrustes Analysis: Transfer Learning for Brain–Computer Interfaces. *IEEE Transactions on Biomedical Engineering*, 66(8):2390–2401, 2019. doi: 10.1109/TBME.2018.2889705.
- Raphaëlle N. Roy, Marcel F. Hinss, Ludovic Darmet, Simon Ladouce, Emilie S. Jahanpour, Bertille Somon, Xiaoqi Xu, Nicolas Drougard, Frédéric Dehais, and Fabien Lotte. Retrospective on the First Passive Brain-Computer Interface Competition on Cross-Session Workload Estimation. *Frontiers in Neuroergonomics*, 3:838342, 2022. doi: 10.3389/fnrgo.2022.838342.
- David Sabbagh, Pierre Ablin, Gaël Varoquaux, Alexandre Gramfort, and Denis A Engemann. Predictive regression modeling with meg/eeg: from source power to signals and cognitive states. *NeuroImage*, 222:116893, 2020. doi: j.neuroimage.2020.116893.
- Robin Tibor Schirmer, Jost Tobias Springenberg, Lukas Dominique Josef Fiederer, Martin Glasstetter, Katharina Eggensperger, Michael Tangermann, Frank Hutter, Wolfram Burgard, and Tonio Ball. Deep learning with convolutional neural networks for eeg decoding and visualization. *Human Brain Mapping*, aug 2017. ISSN 1097-0193. doi: 10.1002/hbm.23730. URL <http://dx.doi.org/10.1002/hbm.23730>.
- Yuan Shi and Fei Sha. Information-theoretical learning of discriminative clusters for unsupervised domain adaptation. In *Proceedings of the 29th International Conference on International Conference on Machine Learning*, pp. 1275–1282, Madison, WI, USA, 2012. Omnipress.
- Nazmi Sofian Suhaimi, James Mountstephens, and Jason Teo. Eeg-based emotion recognition: a state-of-the-art review of current trends and opportunities. *Computational intelligence and neuroscience*, 2020(1):8875426, 2020. doi: 10.1155/2020/8875426.
- Akara Supratak, Hao Dong, Chao Wu, and Yike Guo. Deepsleepnet: A model for automatic sleep stage scoring based on raw single-channel eeg. *IEEE transactions on neural systems and rehabilitation engineering*, 25(11):1998–2008, 2017.
- Michael Tangermann, Klaus-Robert Müller, Ad Aertsen, Niels Birbaumer, Christoph Braun, Clemens Brunner, Robert Leeb, Carsten Mehring, Kai J Miller, Gernot R Müller-Putz, et al. Review of the bci competition iv. *Frontiers in neuroscience*, 6:55, 2012. doi: 10.3389/fnins.2012.00055.
- Mario Giovanni Terzano, Liborio Parrino, Adriano Sherieri, Ronald Chervin, Sudhansu Chokroverty, Christian Guilleminault, Max Hirshkowitz, Mark Mahowald, Harvey Moldofsky, Agostino Rosa, et al. Atlas, rules, and recording techniques for the scoring of cyclic alternating pattern (cap) in human sleep. *Sleep medicine*, 2(6):537–554, 2001. doi: 10.1016/s1389-9457(01)00149-6.
- Philipp Thölke, Yorguin-Jose Mantilla-Ramos, Hamza Abdelhedi, Charlotte Maschke, Arthur Dehgan, Yann Harel, Anirudha Kemtur, Loubna Mekki Berrada, Myriam Sahraoui, Tammy Young, et al. Class imbalance should not throw you off balance: Choosing the right classifiers and performance metrics for brain decoding with imbalanced data. *NeuroImage*, 277:120253, 2023. doi: 10.1016/j.neuroimage.2023.120253.

- Xiaoxi Wei, A. Aldo Faisal, Moritz Grosse-Wentrup, Alexandre Gramfort, Sylvain Chevallier, Vinay Jayaram, Camille Jeunet, Stylianos Bakas, Siegfried Ludwig, Konstantinos Bampas, Mehdi Bahri, Yannis Panagakis, Nikolaos Laskaris, Dimitrios A. Adamos, Stefanos Zafeiriou, William C. Duong, Stephen M. Gordon, Vernon J. Lawhern, Maciej Śliwowski, Vincent Rouanne, and Piotr Tempczyk. 2021 BEETL Competition: Advancing Transfer Learning for Subject Independence and Heterogenous EEG Data Sets. In Douwe Kiela, Marco Ciccone, and Barbara Caputo (eds.), *Proceedings of the NeurIPS 2021 Competitions and Demonstrations Track*, volume 176 of *Proceedings of Machine Learning Research*, pp. 205–219. PMLR, 2022.
- Jonathan R Wolpaw, Niels Birbaumer, Dennis J McFarland, Gert Pfurtscheller, and Theresa M Vaughan. Brain–computer interfaces for communication and control. *Clinical neurophysiology*, 113(6):767–791, 2002. doi: 10.1016/S1388-2457(02)00057-3.
- Edward A Wolpert. A manual of standardized terminology, techniques and scoring system for sleep stages of human subjects. *Archives of General Psychiatry*, 20(2):246–247, 1969. doi: 10.1001/archpsyc.1969.01740140118016.
- Dongrui Wu, Yifan Xu, and Bao-Liang Lu. Transfer learning for eeg-based brain–computer interfaces: A review of progress made since 2016. *IEEE Transactions on Cognitive and Developmental Systems*, 14(1):4–19, 2020. doi: 10.1109/TCDS.2020.3007453.
- Or Yair, Mirela Ben-Chen, and Ronen Talmon. Parallel transport on the cone manifold of spd matrices for domain adaptation. *IEEE Transactions on Signal Processing*, 67(7):1797–1811, 2019. doi: 10.1109/TSP.2019.2894801.
- Shiqi Yang, Yaxing Wang, Joost Van De Weijer, Luis Herranz, and Shangling Jui. Generalized source-free domain adaptation. In *Proceedings of the IEEE/CVF international conference on computer vision*, pp. 8978–8987, 2021.
- Paolo Zanini, Marco Congedo, Christian Jutten, Salem Said, and Yannick Berthoumieu. Transfer learning: A riemannian geometry framework with applications to brain–computer interfaces. *IEEE Transactions on Biomedical Engineering*, 65(5):1107–1116, 2017. doi: 10.1109/TBME.2017.2742541.
- Bangyan Zhou, Xiaopei Wu, Zhao Lv, Lei Zhang, and Xiaojin Guo. A fully automated trial selection method for optimization of motor imagery based brain-computer interface. *PloS one*, 11(9): e0162657, 2016. doi: 10.1371/journal.pone.0162657.

A APPENDIX

A.1 PROOF OF PROPOSITION 1

Proposition 1 states that given the generative model specified in section 3.1 and a set of examples $\mathcal{E}_j = \{(E_i, y_i, j) | E_i \in \mathcal{S}_P^+, y_i \in \mathcal{Y}\}_{i \leq M_j}$ of domain $j \in \mathcal{J}$, we have that the Fréchet mean of \mathcal{E}_j , defined in (2), converges with $M_j \rightarrow \infty$ to the identity matrix I_P for all domains $j \in \mathcal{J}$.

Since $(\mathcal{S}_P^+, g^{\text{AIRM}})$ forms a Cartan-Hadamard manifold with global non-positive sectional curvature, a unique Fréchet mean exists (Bhatia, 2013). At the global minimum, we have:

$$0 \stackrel{!}{=} \nabla_E \nu_E(\mathcal{E}_j) = \nabla_E \frac{1}{M_j} \sum_{i=1}^{M_j} \delta^2(E, E_i) = \frac{1}{M_j} \sum_{i=1}^{M_j} \nabla_E \delta^2(E, E_i) = -\frac{1}{M_j} \sum_{i=1}^{M_j} \text{Log}_E(E_i) \quad (22)$$

$$= -\frac{1}{M_j} \sum_{i=1}^{M_j} E^{\frac{1}{2}} \log(E^{-\frac{1}{2}} E_i E^{-\frac{1}{2}}) E^{\frac{1}{2}} = -\frac{1}{M_j} E^{\frac{1}{2}} \left(\sum_{i=1}^{M_j} \log(E^{-\frac{1}{2}} E_i E^{-\frac{1}{2}}) \right) E^{\frac{1}{2}} \quad (23)$$

$$0 \stackrel{!}{=} \sum_{i=1}^{M_j} \log(E^{-\frac{1}{2}} E_i E^{-\frac{1}{2}}) \quad (24)$$

where we used the derivative of the Riemannian distance (Moakher, 2005; Pennec, 2018) in (22). For $E = I_P$, (24) simplifies to:

$$\sum_{i=1}^{M_j} \log(E_i) \stackrel{!}{=} 0 \implies_{M_j \rightarrow \infty} \mathbb{E}\{\log(E_i)\} \stackrel{!}{=} 0 \quad (25)$$

$$\mathbb{E}\{B\tilde{y}_i + \varepsilon_i\} = B\mathbb{E}\{\tilde{y}_i\} + \mathbb{E}\{\varepsilon_i\} \stackrel{!}{=} 0 \quad (26)$$

which holds true because by definition \tilde{y}_i and ε_i are zero-mean. Therefore, $E_j = I_P$ is the global minimizer of $\nu_E(\mathcal{E}_j)$ for all domains $j \in \mathcal{J}$. \square

A.2 PROOF OF PROPOSITION 2

Proposition 2 states that for the generative model, specified in section 3.1, RCT+TSM compensates conditional distribution shifts introduced by the invertible linear map A_j , defined in (8), and recovers domain-invariant representations if there are no target shifts (i.e., $p_j(y=y) = p(y=y) \forall y \in \mathcal{Y}, \forall j \in \mathcal{J}_s \cup \mathcal{J}_t$).

Due to the congruence invariance of the Fréchet mean (Bhatia, 2013) we have

$$\bar{C}_j = \arg \min_{G \in \mathcal{S}_P^+} \nu_G(\mathcal{C}_j) = A_j \bar{E}_j A_j^T \quad (27)$$

where \bar{E}_j is the Fréchet mean of \mathcal{E}_j . Utilizing proposition 1 (i.e., $\bar{E}_j = I_P \forall j$) and plugging in (9) for A_j , (27) simplifies to:

$$\bar{C}_j = A_j I_P A_j^T = Q \exp(P_j) \exp(P_j) Q^T = Q \exp(P_j)^2 Q^T \quad (28)$$

$$\Rightarrow \bar{C}_j^{-\frac{1}{2}} = Q \exp(P_j)^{-1} Q^T \quad (29)$$

The RCT+TSM transform, as defined in (14), recenters the data $C_i \in \mathcal{C}_j$ for each domain j . Excluding the invertible mapping upper, RCT+TSM computes:

$$\log \left(\bar{C}_j^{-\frac{1}{2}} C_i \bar{C}_j^{-\frac{1}{2}} \right) = \log \left(Q \exp(P_j)^{-1} Q^T C_i Q \exp(P_j)^{-1} Q^T \right) \quad (30)$$

$$= \log \left(Q \exp(P_j)^{-1} A_j E_i A_j^T \exp(P_j)^{-1} Q^T \right) \quad (31)$$

$$= \log \left(Q \exp(P_j)^{-1} Q^T Q \exp(P_j) E_i \exp(P_j) Q^T Q \exp(P_j)^{-1} Q^T \right) \quad (32)$$

$$= \log \left(Q E_i Q^T \right) = Q \log(E_i) Q^T \quad (33)$$

where we used (13) for C_i , the fact that Q is an orthogonal matrix and $\log(ACA^{-1}) = A \log(C)A^{-1}$ for non-singular A and $C \in \mathcal{S}_P^+$. Plugging (11) for $\log(E_i)$, we obtain a direct relationship to the label y_i

$$\log\left(\bar{C}_j^{-\frac{1}{2}} C_i \bar{C}_j^{-\frac{1}{2}}\right) = Q_{\text{upper}}^{-1} (B(1_{y_i} - \pi_j) + \varepsilon_i) Q^T \quad (34)$$

If there are no target shifts the class priors are constant $p_j(y=y) = p(y=y) \forall y \in \mathcal{Y}$ for all domains $j \in \mathcal{J}_s \cup \mathcal{J}_t$, and consequently $\pi_j = \pi$. Then (34) simplifies to:

$$\log\left(\bar{C}_j^{-\frac{1}{2}} C_i \bar{C}_j^{-\frac{1}{2}}\right) = Q_{\text{upper}}^{-1} (B(1_{y_i} - \pi) + \varepsilon_i) Q^T \quad (35)$$

which contains only domain-invariant terms on the right hand side. Thus, RCT+TSM compensates the conditional shifts introduced by A_j . \square

A.3 SLEEP STAGE DATASET DETAILS

Dataset	Recordings	Subjects	Channel numbers	Patients	Scorer	Scoring rule
ISRUC-SG1	100	100	6	✓	Scorer1	AASM
ISRUC-SG2	16	8	6	✓	Scorer1	AASM
ISRUC-SG3	10	10	6	✗	Scorer1	AASM
Dreem-SG1	22	22	12	✗	Scorer1	AASM
Dreem-SG2	50	50	8	✓	Scorer1	AASM
HMC	154	154	4	✓	-	AASM
CAP-SG1	36	36	13	✓	-	K&M
CAP-SG2	34	34	9	✓	-	K&M
CAP-SG3	22	22	5	✓	-	K&M

Table A1: **Sleep stage dataset details.** Overview of datasets and their subgroups (SG), including the number of recordings, subjects, channel numbers, patient status, scorer (the chosen scorer if there are multiple scorers), and scoring rule.

A.4 EEG-BASED SLEEP STAGING RESULTS

Model	Dataset:	Group:	CAP		Dreem		HMC	ISRUC		Overall	
			patient (n=82)	healthy (n=22)	patient (n=50)	patient (n=154)	healthy (n=10)	patient (n=108)	healthy (n=32)	patient (n=394)	
Chambon	w/o	mean	64.7	65.2	53.4	64.0	72.7	68.9	67.5	64.2	
		std	10.7	9.1	16.2	9.6	3.9	8.2	8.6	11.5	
		t-val	• -6.8	• -5.3	• -6.1	• -7.0	-2.6	• -4.6	• -5.8	• -11.3	
	EA	mean	63.8	64.7	54.5	63.4	74.9	70.7	67.9	64.3	
		std	11.3	10.3	14.4	10.7	4.8	9.3	10.0	12.0	
		t-val	• -7.5	• -3.8	• -6.1	• -7.5	-1.2	-1.3	• -3.8	• -10.7	
	STMA	mean	65.2	67.1	51.3	63.8	74.8	70.8	69.5	64.4	
		std	10.0	7.7	19.0	9.1	4.4	7.6	7.7	12.1	
		t-val	• -8.5	• -5.0	• -6.0	• -8.6	-1.3	-1.4	• -4.7	• -10.4	
USleep	w/o	mean	59.1	55.9	48.4	66.6	72.9	68.8	61.3	63.3	
		std	10.3	8.3	8.2	9.3	6.1	8.3	11.0	11.3	
		t-val	• -12.1	• -8.0	• -13.3	• -2.8	-2.2	• -4.3	• -6.8	• -12.1	
DeepSleepNet	w/o	mean	68.1	68.6	68.7	64.9	75.8	72.7	70.9	68.2	
		std	11.3	9.9	10.3	10.3	4.5	9.1	9.1	10.7	
		t-val	• -3.3	• -3.1	0.5	• -5.1	-0.5	1.7	-2.8	• -3.9	
	EA	mean	66.4	66.3	62.3	67.1	74.1	73.2	68.8	68.0	
		std	11.7	10.3	11.4	10.2	4.6	9.9	9.6	11.1	
		t-val	• -5.1	• -3.1	• -3.6	-2.3	• -4.1	2.1	• -3.6	• -4.1	
	STMA	mean	67.7	70.5	64.2	64.8	74.5	72.9	71.8	67.6	
		std	10.1	8.5	11.4	10.2	4.0	7.8	7.5	10.3	
		t-val	• -4.7	-1.4	-2.7	• -5.5	-1.3	2.5	-1.9	• -5.8	
AttnSleep	w/o	mean	68.9	65.4	61.7	67.7	75.4	73.1	68.5	68.7	
		std	10.3	10.7	14.2	10.0	4.0	8.6	10.2	10.9	
		t-val	-2.6	• -4.4	• -3.1	-1.4	-1.3	2.2	• -4.3	-2.6	
	EA	mean	68.6	65.5	59.6	65.7	75.4	74.2	68.6	67.9	
		std	11.7	11.1	15.3	11.1	4.5	7.1	10.5	11.9	
		t-val	• -2.9	• -3.4	• -3.9	• -3.9	-1.0	• 4.5	• -3.4	• -4.0	
	STMA	mean	69.9	69.0	61.8	66.8	75.7	74.6	71.1	68.9	
		std	10.2	8.8	14.8	9.4	3.9	7.0	8.2	10.7	
		t-val	-1.7	-2.9	• -3.0	• -3.3	-0.8	• 5.2	-2.9	-2.2	
TSMNet	w/o	mean	68.0	65.9	66.7	63.6	73.4	68.7	68.3	66.3	
		std	11.2	9.6	12.4	11.3	3.9	9.3	8.9	11.1	
		t-val	• -3.7	• -6.5	-1.0	• -6.8	• -3.4	• -3.8	• -7.0	• -8.2	
	EA	mean	67.5	66.7	67.0	62.1	73.3	68.1	68.7	65.5	
		std	9.9	11.2	11.1	12.0	2.2	9.7	9.8	11.2	
		t-val	• -4.3	• -3.4	-0.8	• -8.2	-3.3	• -4.3	• -4.2	• -9.5	
	STMA	mean	69.9	70.7	68.2	65.0	73.4	69.2	71.5	67.6	
		std	9.6	7.7	10.6	9.0	5.1	7.9	7.1	9.2	
		t-val	-1.8	-1.5	0.1	• -7.3	-1.9	• -4.8	-2.4	• -7.3	
SPDDBSN	mean	68.2	68.9	64.2	62.2	72.8	66.6	70.1	64.9		
	std	8.8	5.8	8.5	6.0	2.8	6.4	5.3	7.5		
	t-val	• -6.3	• -4.8	• -8.6	• -15.3	• -3.8	• -13.4	• -6.2	• -21.4		
SPDIM(bias)	mean	71.0	72.1	68.1	68.6	76.7	71.6	73.5	69.9		
	std	9.6	8.0	9.8	8.5	3.4	6.9	7.2	8.6		
	t-val	-	-	-	-	-	-	-	-		

Table A2: **Sleep-staging results per dataset.** Summary statistics of the test-set scores (balanced accuracy; higher is better) across public sleep staging datasets. Parameters that were adapted to the test-data with the IM loss are indicated in brackets. Permutation-paired t-tests were used to identify significant differences between our *proposed* (i.e., TSMNet+SPDIM(bias)) and baseline methods (1e4 permutations, 10 tests, t-max correction). Student’s t values summarize the effect strength. Significant differences are highlighted (• $p \leq 0.05$, • $p \leq 0.01$, • $p \leq 0.001$).

Alignment / Mean	$\mathcal{L}_{IM} / \Theta_{IM}$	Dataset: Group:	CAP		Dreem		HMC	ISRUC		Overall	
			patient (n=82)	healthy (n=22)	patient (n=50)	patient (n=154)	healthy (n=10)	patient (n=108)	healthy (n=32)	patient (n=394)	
m_ϕ (19) / per domain j	✓ / Φ_j	mean	71.0	72.1	68.1	68.6	76.7	71.6	73.5	69.9	
		std	9.6	8.0	9.8	8.5	3.4	6.9	7.2	8.6	
		t-val	-	-	-	-	-	-	-	-	-
$m_\phi^\#$ (20) per domain j	✓ / φ_j	mean	68.6	70.0	66.8	64.7	74.6	68.3	71.4	66.8	
		std	9.2	6.6	9.0	7.1	3.2	6.4	6.1	7.8	
		t-val	• -6.4	• -3.9	• -3.7	• -12.2	• -3.9	• -10.0	• -5.3	• -16.8	
\tilde{m}_ϕ (14) per domain j	✗ / -	mean	68.2	68.9	64.2	62.2	72.8	66.6	70.1	64.9	
		std	8.8	5.8	8.5	6.0	2.8	6.4	5.3	7.5	
		t-val	• -6.3	• -4.8	• -8.6	• -15.3	• -3.8	• -13.4	• -6.2	• -21.4	
\tilde{m}_ϕ (14) global	✗ / -	mean	68.0	65.9	66.7	63.6	73.4	68.7	68.3	66.3	
		std	11.2	9.6	12.4	11.3	3.9	9.3	8.9	11.1	
		t-val	• -3.7	• -6.5	-1.0	• -6.8	• -3.4	• -3.8	• -7.0	• -8.2	
\tilde{m}_ϕ (14) per domain j	✓ / bias in ψ	mean	69.8	70.3	65.7	64.1	74.7	68.9	71.7	66.8	
		std	9.5	6.8	9.2	6.9	2.7	6.8	6.1	8.1	
		t-val	• -3.3	• -4.0	• -7.4	• -13.0	• -3.9	• -8.1	• -5.4	• -15.6	
\tilde{m}_ϕ (14) per domain j	✓ / ψ	mean	67.4	68.8	63.1	62.3	73.2	67.7	70.2	64.9	
		std	10.5	8.5	10.9	9.8	5.0	8.8	7.7	10.1	
		t-val	• -5.9	• -3.1	• -6.1	• -14.5	• -3.8	• -8.6	• -4.3	• -18.0	
\tilde{m}_ϕ (14) per domain j	✓ / $\theta \cup \psi$	mean	54.8	46.9	36.2	35.8	53.6	45.9	49.0	42.5	
		std	14.8	13.8	11.4	11.2	13.4	12.5	13.8	14.5	
		t-val	• -13.3	• -9.6	• -17.1	• -32.8	• -6.4	• -23.0	• -11.6	• -39.9	

Table A3: **Sleep-staging ablation study results per dataset.** Summary statistics (mean, std, t-val) of the test-set scores (balanced accuracy; higher is better) across public sleep staging datasets. All statistics are computed at the subject level. Permutation-paired t-tests were used to identify significant differences (1e4 permutations, 6 tests, t-max correction). Significant differences are highlighted (• $p \leq 0.05$, • $p \leq 0.01$, • $p \leq 0.001$). For a summary across datasets and groups see Table 3 in the main manuscript.

A.5 EEG-BASED MOTOR IMAGERY BCI

label ratio = 0.2												
Model	SFUDA	Evaluation : Dataset :	session				Overall (n=34)	subject				Overall (n=34)
			2014001 (n=9)	2014004 (n=9)	2015001 (n=12)	Zhou2016 (n=4)		2014001 (n=9)	2014004 (n=9)	2015001 (n=12)	Zhou2016 (n=4)	
EEGNet v4	w/o	mean	41.1	74.5	72.4	71.7	64.6	42.6	69.0	61.4	72.6	59.7
		std	17.9	14.6	16.3	5.8	20.6	16.6	10.7	8.3	3.7	15.6
		t-val	• -4.8	0.2	• -4.1	-4.4	• -5.0	• -4.3	-1.7	-2.3	-3.4	• -4.2
	EA	mean	53.2	75.3	76.0	77.2	69.9	48.6	72.0	70.7	70.6	65.2
		std	21.8	15.4	18.3	2.9	19.7	17.2	11.1	14.7	6.8	16.7
		t-val	• -5.2	0.8	-2.7	-8.9	• -4.4	-1.9	-0.1	-0.5	-3.2	-1.5
	STMA	mean	28.9	73.8	55.5	67.1	54.7	50.0	71.7	68.5	73.1	65.0
		std	5.5	14.4	9.5	14.5	20.2	16.1	12.4	14.3	2.2	16.0
		t-val	• -7.3	-0.2	• -8.3	-2.4	• -6.8	-1.6	-0.2	-0.8	-9.1	-1.5
EEG- Conformer	w/o	mean	48.6	75.0	71.6	73.9	66.7	41.7	69.4	60.6	74.6	59.6
	std	17.0	11.4	18.5	3.8	18.4	15.2	10.9	11.7	6.0	16.6	
	t-val	• -6.1	0.5	• -4.0	-6.2	• -5.5	• -4.1	-1.7	-2.4	-2.8	• -4.1	
ATCNet	w/o	mean	52.2	74.7	72.8	80.3	68.7	41.6	68.4	59.8	67.5	58.2
	std	18.7	13.8	16.3	4.3	18.1	16.3	10.9	8.7	8.7	15.5	
	t-val	-4.0	0.3	• -3.8	-2.3	• -4.5	• -4.8	-3.1	-2.9	-3.9	• -5.3	
EEGIn ceptionMI	w/o	mean	47.7	71.5	72.6	75.1	66.0	39.4	67.0	59.2	63.1	56.5
	std	17.0	12.1	15.8	9.4	18.0	13.8	9.5	9.5	6.4	14.8	
	t-val	• -6.1	-1.2	• -4.9	-1.9	• -6.1	-3.5	-2.3	-2.5	-6.9	• -4.9	
TSMNet	w/o	mean	68.6	74.8	82.7	81.0	76.7	41.1	69.5	61.1	77.8	60.0
		std	12.9	11.1	13.4	2.5	12.8	12.7	9.6	10.9	2.6	16.2
		t-val	-0.5	0.4	-0.6	-1.8	-0.9	• -4.3	-1.5	-2.0	-1.3	• -3.5
	EA	mean	67.2	76.0	83.6	81.9	77.0	50.0	73.0	68.2	73.3	65.3
		std	13.7	12.0	9.5	5.2	12.6	16.9	10.6	13.7	4.3	15.9
		t-val	-1.2	2.1	-0.1	-0.9	-0.6	-1.4	0.5	-0.9	-2.4	-1.5
	STMA	mean	69.9	74.7	83.0	83.3	77.3	50.2	71.9	66.9	76.8	65.0
		std	16.0	13.1	7.7	6.3	12.7	17.5	11.5	13.0	5.5	16.0
		t-val	0.1	0.4	-0.3	-0.4	-0.2	-1.4	-0.2	-1.2	-1.2	-1.7
	IM (classifier bias)	mean	69.9	74.2	83.2	78.3	76.7	52.9	70.6	73.0	75.4	67.3
		std	17.5	12.5	10.1	3.0	13.3	15.0	9.9	15.1	3.8	15.3
		t-val	0.2	-0.0	-0.6	-11.2	-1.7	0.4	-1.0	-0.7	-1.7	-1.7
	IM (classifier)	mean	66.6	70.9	78.2	77.0	73.0	50.5	67.0	69.7	69.0	63.8
		std	17.2	9.5	6.6	1.7	11.5	14.9	9.1	12.4	7.5	14.1
		t-val	-3.1	-3.0	• -3.8	-17.2	• -6.8	-1.1	• -4.1	• -3.9	-2.9	• -5.0
	IM (all)	mean	37.9	50.9	70.8	55.4	55.0	36.0	50.4	63.2	56.0	51.8
		std	10.9	1.7	7.8	6.4	15.1	7.5	1.7	8.3	4.1	12.5
		t-val	• -6.6	• -6.1	• -4.0	-7.5	• -9.5	• -4.0	• -5.2	-2.5	-10.3	• -7.3
	SPDDBSN	mean	69.3	73.5	81.2	80.6	76.0	52.1	69.6	71.5	76.2	66.4
		std	16.2	11.0	8.6	2.4	12.0	13.9	9.8	13.5	3.1	14.5
		t-val	-0.3	-0.9	-2.4	-7.0	-2.8	-0.3	-1.9	-2.6	-1.9	• -3.2
	SPDIM (geodesic)	mean	70.0	74.7	83.7	82.6	77.6	52.3	70.9	73.4	78.4	67.7
		std	16.5	11.9	10.3	3.5	13.1	15.1	10.9	15.2	3.6	16.0
		t-val	0.4	0.8	0.1	-1.4	0.1	-0.3	-1.4	-0.3	-1.1	-1.6
	SPDIM (bias)	mean	69.7	74.3	83.6	84.1	77.5	52.6	72.2	73.6	80.4	68.5
		std	18.4	12.2	10.6	2.2	13.9	16.5	12.0	14.8	2.4	16.6
		t-val	-	-	-	-	-	-	-	-	-	-

Table A4: **Motor imagery BCI results for a label ratio of 0.2.** Average and standard deviation of test-set scores (balanced accuracy; higher is better) across public motor imagery BCI datasets. For all IM and SPDIM variants, the parameters that were tuned to the test-data with the IM loss are indicated in brackets. Permutation-paired t-tests were used to identify significant differences between the *proposed* (i.e., TSMNet+SPDIM(bias)) and baseline methods (1e4 permutations, 14 tests, t-max correction). Student’s t values summarize the effect strength. Significant differences are highlighted ($\bullet p \leq 0.05$, $\bullet p \leq 0.01$, $\bullet p \leq 0.001$).

label ratio = 1.0												
Model	SFUDA	Evaluation :					subject					
		Dataset :	2014001 (n=9)	2014004 (n=9)	session 2015001 (n=12)	Zhou2016 (n=4)	Overall (n=34)	2014001 (n=9)	2014004 (n=9)	2015001 (n=12)	Zhou2016 (n=4)	Overall (n=34)
EEGNet v4	w/o	mean	41.0	73.1	73.5	70.6	64.4	43.6	69.6	61.3	75.1	60.4
		std	16.6	15.0	15.8	6.5	20.3	16.7	8.1	8.8	3.2	15.4
		t-val	• -6.5	• -3.6	• -4.7	-3.8	• -6.3	• -5.0	-2.1	-2.4	-2.8	• -4.4
	EA	mean	54.5	76.3	75.7	79.6	70.7	49.9	74.0	72.5	73.9	67.1
		std	19.9	15.5	17.1	2.9	18.7	16.9	10.4	14.2	3.7	16.6
		t-val	• -6.3	-1.0	• -3.7	-4.9	• -5.5	-3.4	1.5	-0.3	-4.8	-1.2
	STMA	mean	30.1	74.4	55.9	68.3	55.4	49.7	72.6	69.9	75.0	65.9
		std	4.7	15.8	8.0	16.8	20.1	16.9	10.6	14.6	2.4	16.4
		t-val	• -9.4	-1.8	• -9.9	-1.8	• -7.6	• -3.7	-0.8	-0.7	-4.9	-1.6
EEG- Conformer	w/o	mean	46.9	73.8	73.1	71.1	66.1	42.6	68.8	60.1	74.5	59.5
		std	17.2	12.8	17.2	3.2	18.7	16.7	10.0	10.7	4.4	16.1
		t-val	• -8.9	• -3.6	• -4.5	-8.5	• -7.2	• -5.0	-2.8	-2.6	-4.1	• -4.7
ATCNet	w/o	mean	51.6	74.3	73.2	77.9	68.3	42.7	68.5	60.2	69.8	58.9
		std	18.4	13.8	15.6	4.3	17.8	16.4	8.9	8.4	6.3	14.9
		t-val	• -5.6	-3.0	• -4.7	-3.0	• -6.3	• -5.7	• -3.6	-2.8	-4.6	• -5.5
EEGInc- ceptionMI	w/o	mean	49.1	71.7	73.1	72.3	66.3	39.7	67.3	59.5	67.6	57.3
		std	17.9	12.6	15.7	8.5	17.7	12.7	8.1	9.2	5.4	14.6
		t-val	• -7.3	• -3.8	• -5.6	-2.6	• -7.7	• -5.1	-2.8	-2.5	-5.2	• -5.2
TSMNet	w/o	mean	69.7	75.1	82.2	80.0	76.8	43.0	68.0	61.7	77.5	60.3
		std	11.8	11.2	12.9	2.0	12.1	13.3	9.3	11.4	3.7	15.6
		t-val	-2.6	-2.4	-2.0	-5.3	• -4.6	• -6.0	-3.2	-2.0	-1.7	• -3.9
	EA	mean	71.1	77.1	85.2	83.8	79.2	51.2	73.1	72.5	75.0	67.3
		std	13.3	12.8	9.7	2.6	12.2	15.1	11.1	13.6	1.8	15.6
		t-val	-2.1	-0.5	-0.0	-1.0	-1.8	-1.6	-0.6	-0.3	-8.1	-1.1
	STMA	mean	71.9	76.3	84.9	82.8	78.9	52.5	72.5	70.1	77.1	66.9
		std	15.2	13.3	9.2	3.0	12.6	16.4	11.3	14.2	1.9	15.6
		t-val	-1.6	-2.4	-0.3	-4.3	-2.0	-1.7	-1.3	-0.7	-4.0	-1.3
	SPDDBN	mean	73.7	77.4	85.3	84.6	80.0	54.6	73.3	74.3	80.9	69.6
		std	15.3	12.5	10.4	2.3	12.5	16.1	11.1	14.7	1.5	15.9
		t-val	-	-	-	-	-	-	-	-	-	-

Table A5: **Motor imagery BCI results for balanced data (i.e., label ratio of 1.0).** Average and standard deviation of test-set scores (balanced accuracy; higher is better) across public motor imagery BCI datasets. For all IM and SPDIM variants, the parameters that were tuned to the test-data with the IM loss are indicated in brackets. Permutation-paired t-tests were used to identify significant differences between the *TSMNet+SPDDBN* and baseline methods (1e4 permutations, 9 tests, t-max correction). Student’s t values summarize the effect strength. Significant differences are highlighted (• $p \leq 0.05$, • $p \leq 0.01$, • $p \leq 0.001$).

A.6 SIMULATIONS

A.6.1 IMPLEMENTATION DETAILS

We generated covariance matrices $C_i \in \mathcal{S}_P^+$ with $P = 2$. To do so, we first generated log-space features $s_i \in \mathbb{R}^{P(P+1)/2}$, defined in (11), using the scikit-learn function `make_classification` with 2 dimensions encoding label information. The data were then normalized to have zero mean and unit variance. To obtain $E_i \in \mathcal{S}_P^+$, we applied upper^{-1} and Exp_{I_P} , as defined in (5). At this level, the data were split across source domains and the target domain, with each domain receiving 500 observations. Finally, the data were projected to the channel space using domain-specific mixing matrices A_j , as defined in (9). To introduce label shifts, we artificially varied the label ratio (LR), defined as the proportion of the minority class to the majority class, in the target domain via randomly dropping samples.

We used balanced accuracy as evaluation metric and examined the performance of SPDIM(bias) and SPDIM(geodesic) against RCT (Zanini et al., 2017) over different label ratios. Figure 2 summarizes the results for different SNR levels. To control the SNR, we varied the class separability parameter of the `make_classification` function. Additional Figures summarize the methods’ performance over parameters $|\mathcal{J}_s|$ (Figure A1), M_j (Figure A2), P (Figure A3), and D (Figure A4).

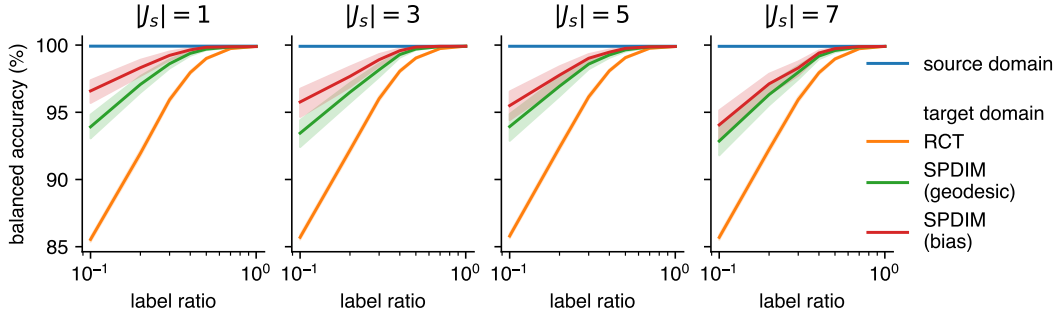


Figure A1: **Performance over the number of source domains.** Same parameters as in Figure 2 (panel 3) but for a different number of source domains $|\mathcal{J}_s| \in \{1, 3, 5, 7\}$.

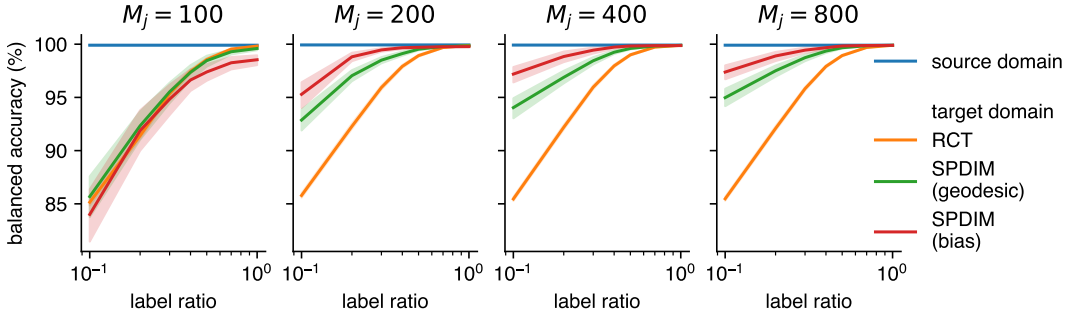


Figure A2: **Performance over the number of samples per domain M_j .** Same as Figure 2 (panel 3) but for a different number of samples per domains $M_j \in \{100, 200, 400, 800\}$.

A.7 IMPLEMENTATION DETAILS

A.7.1 TSMNET

We used the TSMNet as provided in the public reference implementation as follows:

Architecture The feature extractor f_θ has two convolutional layers, followed by covariance pooling (Acharya et al., 2018), BiMap (Huang & Gool, 2017), and ReEig Huang & Gool (2017) layers. The first convolutional layer operates convolution along the temporal dimension, implementing a

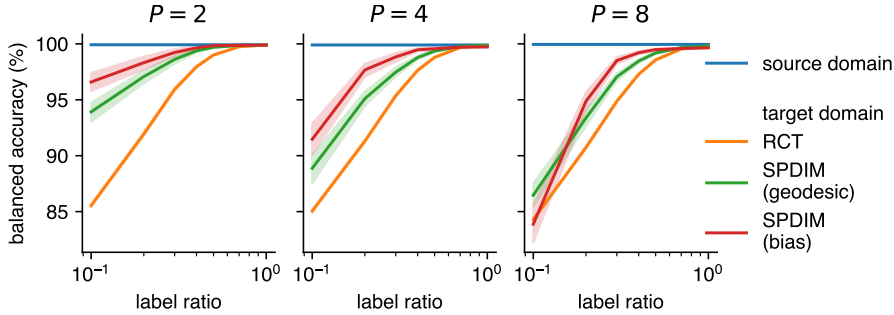


Figure A3: **Performance over the number of dimensions P .** Same parameters as in Figure 2 (panel 3) but for a different number of dimensions $P \in \{2, 4, 8\}$.

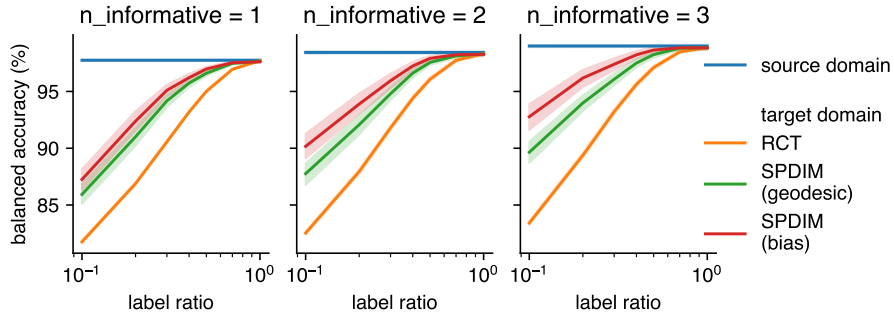


Figure A4: **Performance over the number of informative sources.** Same as Figure 2 (panel 3) but for a different number of informative dimensions encoding label information in s , as defined in (11). The $n_informative$ parameter of the scikit-learn function `make_classification` effectively defines the dimensionality of the label encoding subspace D .

finite impulse response (FIR) filter bank (4 filters) with learnable parameters. The second convolutional layer applies spatio-spectral filters (40 filters) along the spatial and convolutional channel dimensions. Covariance pooling is then applied along the temporal dimension. A subsequent BiMap layer projects covariance matrices to a D -dimensional subspace ($D-20$) via bilinear mapping. Next, a ReEig layer rectifies all eigenvalues lower than a threshold 10^{-4} . We varied the alignment and tangent space mapping layer m_ϕ as specified in the main text. Finally, the classification head g_ψ is parametrized as a linear layer with softmax activations.

Parameter estimation We used the cross-entropy loss as the training objective, employing the PyTorch framework (Paszke et al., 2019) with extensions for structured matrices (Ionescu et al., 2015) and manifold-constrained gradients (Absil et al., 2008) to propagate gradients through the layers. We stick to the hyper-parameters as provided in the public reference implementation. Specifically, gradients were estimated using fixed-size mini-batches (50 observations; 10 per domain across 5 domains) and updated parameters with the Riemannian ADAM optimizer (Bécigneul & Ganea, 2018) (10^{-3} learning rate, 10^{-4} weight decay, $\beta_1 = 0.9$, $\beta_2 = 0.999$). We split the source domains' data into training and validation sets (80% / 20% splits, randomized, stratified by domain and label) and iterated through the training set for 100 epochs using exhaustive minibatch sampling. After training, the model with minimal loss on the validation data was selected.

A.7.2 SLEEP STAGING MODEL

We considered four baseline deep learning architectures Chambon (Chambon et al., 2018), Usleep (Perslev et al., 2021), DeepSleepNet (Supratak et al., 2017), and AttnNet (Eldele et al., 2023) here. Although DeepSleepNet and AttnNet are initially proposed for a single-channel EEG data, there are many related studies (Guillot et al., 2020; Ji et al., 2023; Ma et al., 2024; Guillot & Thorey, 2021) use the model proposed for single-channel data as a baseline for multi-channels data. We use the implementation provided in braindecode (Schirrneister et al., 2017) for all architectures above, and stick to all model hyper-parameters as provided in the braindecode. We used similar learning-related hyper-parameters with an Adam optimizer (e.g., early stopping, no LR scheduler, same batch size,

similar number of epochs) to TSMNet A.7.1. We split the source domains' data into training and validation sets (80% / 20% splits, randomized, stratified by domain and label), and the model with minimal loss on the validation data was selected after training.